Yang, G., Yin, H., Schiffer, C., Brune, S., Jia, D., Wang, W. (2025):
Crustal Heterogeneity Controls the Along-Strike Segmentation:
Analog and Numerical Models of the Northern South China Sea.
- Tectonics, 44, 6, e2024TC008541.

https://doi.org/10.1029/2024TC008541

Tectonics®

RESEARCH ARTICLE
10.1029/2024TC008541

Key Points:

- Lithospheric models provide 3D dynamic insight into how a Mesozoic magmatic arc fundamentally controls the segmentation of northern South China Sea
- The northwestern magmatic arc zone has experienced greater deformation, leading to notably thinner crust than the northeastern forearc basin zone
- Reactivation of pre-existing fault zone between segments during the extensional phase acts as a transfer fault zone, regulating fault displacement

Supporting Information:

Supporting Information may be found in the online version of this article.

Correspondence to:

H. Yin,
hwyin@nju.edu.cn

Citation:

Yang, G., Yin, H., Schiffer, C., Brune, S., Jia, D., & Wang, W. (2025). Crustal heterogeneity controls the along-strike segmentation: Analog and numerical models of the northern South China Sea. *Tectonics*, *44*, e2024TC008541. https://doi.org/10.1029/2024TC008541

Received 6 AUG 2024
Accepted 25 MAY 2025

Author Contributions:

Conceptualization: Gengxiong Yang, Hongwei Yin
Data curation: Gengxiong Yang, Christian Schiffer
Formal analysis: Gengxiong Yang, Christian Schiffer, Wei Wang
Funding acquisition: Hongwei Yin
Investigation: Gengxiong Yang, Hongwei Yin
Methodology: Gengxiong Yang, Sascha Brune, Dong Jia, Wei Wang
Project administration: Hongwei Yin
Software: Christian Schiffer, Sascha Brune
Supervision: Hongwei Yin, Dong Jia
Validation: Christian Schiffer, Dong Jia
Visualization: Gengxiong Yang, Sascha Brune
Writing – original draft: Gengxiong Yang

Crustal Heterogeneity Controls the Along-Strike Segmentation: Analog and Numerical Models of the Northern South China Sea

Gengxiong Yang[1], Hongwei Yin[1], Christian Schiffer[2], Sascha Brune[3,4], Dong Jia[1], and Wei Wang[1]

[1]School of Earth Science and Engineering, Nanjing University, Nanjing, China, [2]Department of Earth Sciences, Uppsala University, Uppsala, Sweden, [3]GFZ Helmholtz Centre for Geosciences, Potsdam, Germany, [4]Institute of Geosciences, University of Potsdam, Potsdam, Germany

Abstract Inherited rheological structure of the lithosphere is expected to exert a significant influence on the architecture of continental rift systems. The eastern and western segments of the northern continental margin of the South China Sea (SCS) exhibit distinct differences in terms of thinning degree, structural style, and magmatic activity. In this paper, we combine 3D analog and 2D numerical models to investigate the influence of lithospheric heterogeneity caused by Mesozoic magmatism on the segmentation of this region. The analog and numerical modeling results, viewed from top and cross-sectional perspectives show that the northwestern margin, characterized by a Mesozoic magmatic arc, experienced greater deformation, resulting in a notably thinner crust compared to the northeastern margin hosting a forearc basin. This difference demonstrates that the local inherited lithospheric heterogeneities along the margin play a fundamental role in controlling the rift-related segmentation of the margin. Furthermore, our analog experiments successfully reproduce a scenario where a pre-existing NW-trending fault zone separates the northeastern and northwestern margins of the SCS, elucidating its role in the differential extension process of the region. This zone acted as a transfer fault zone, adjusting fault displacement and fault spacing in response to differential extension. Numerical simulations complement analog models incorporating variable lithospheric rheology between the northwestern and northeastern segments, providing, for the first time, three-dimensional dynamic insights into how pre-existing lithospheric heterogeneity controlled the temporal evolution and characteristic deformation of the northern SCS margin. These findings have major implications for structural styles and thinning processes in passive rift margins in the presence of crustal heterogeneity.

Plain Language Summary This research explores how crustal heterogeneity, resulting from Mesozoic magmatism, controls the structural segmentation of the northern South China Sea (SCS). Using a series of scaled analog and numerical models, the study demonstrates that strength variations within the lithosphere significantly influenced the differential deformation patterns observed in the northern SCS. The experiments reveal that the northwestern segment, characterized by its Mesozoic magmatic arc, underwent more intense deformation compared to the northeastern segment, characterized by a forearc basin. Specifically, the lithosphere undergoes rapid thinning in the Mesozoic magmatic arc zone, while thinning occurs more gently in the forearc zone. This suggests that the pre-existing magmatic arc and forearc basin zones influenced the differential thinning of the northern SCS. A reactivated NNW-trending transfer fault zone between the northwestern and northeastern segments, also played a key role during the extensional phase.

1. Introduction

The South China Sea (SCS) region (Figure 1a) has undergone a transition from an active to a passive continental margin (Ding et al., 2020; Sun et al., 2019; Zhou et al., 1995). Previous studies using ocean bottom seismometer and multi-channel seismic surveys have extensively investigated the margin's structure, crustal nature, and its tectonic evolution, with a particular focus on the breakup mechanism of the SCS (Deng et al., 2020; Hayes & Nissen, 2005; Wan et al., 2019; Wang et al., 2023; Yan et al., 2001; J. Y. Zhang, Zhao, Sun, et al., 2023; J. Z. Zhang, Zhao, Ding, et al., 2023; Zhao et al., 2019). These studies have yielded a valuable collection of geological and geophysical data, revealing along-strike structural segmentation of the continental margin, including extensional widths of the deformed zone (Figure 1a), margin types, deformation styles, subsidence patterns

10.1029/2024TC008541

Writing – review & editing:
Hongwei Yin, Christian Schiffer

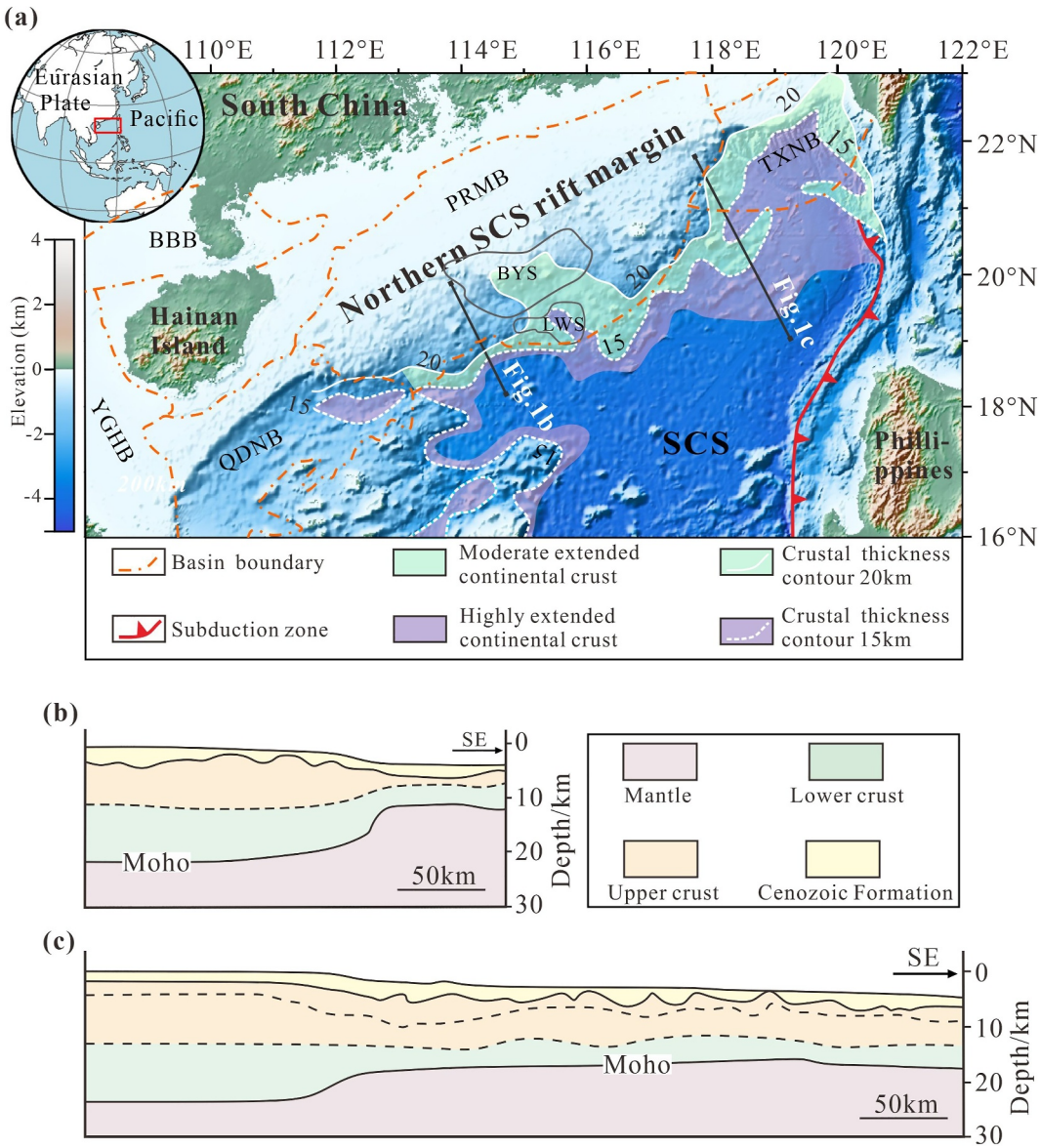

Figure 1. (a) Combined topographic and bathymetric map of the northern South China Sea, with location indicated in the inset. The highly extended continental crust (purple) is from Li et al. (2019). Moderate extended continental crust is defined as the area between crustal contours of 15 and 20 km (light green, Li et al., 2019). Orange dashed lines represent the boundary of the marginal basins. BBB, Beibu Gulf Basin. YGHB, Yinggehai Basin. QDNB, Qiongdongnan Basin. PRMB, Pearl River Mouth Basin. TXNB, Taixinan Basin. SCS, South China Sea. BYS, Baiyun Sag. LWS, Liwan Sag. (b) Schematic interpretation of seismic section illustrating the thinning feature of the northwestern margin (location shown in (panel a)), modified from Wu et al. (2012). (c) Schematic interpretation of seismic section (OBS2001) illustrating the thinning feature of the northeastern margin (location shown in panel a), modified from Li et al. (2019) and Wang et al. (2006).

(Figures 1b and 1c), and Cenozoic magmatic activity. However, three-dimensional (3D) dynamic constraints on rift segmentation along the SCS margin are lacking.

The northern margin of the SCS can be subdivided into two distinct segments: a northwestern magmatic arc zone and a northeastern forearc basin zone, based on different tectono–metamorphic events they were affected by (Figure 2) (Franke, 2013; Savva et al., 2014). Previous studies based on the analysis of magnetic anomalies suggest that the breakup locations of the northeastern and northwestern margins of SCS may have been controlled by different mechanisms: the northeastern margin was likely influenced by the reactivation of the remnant Mesozoic forearc basin, whereas the northwestern margin developed along the remnant magmatic arc (Figure 2)

10.1029/2024TC008541

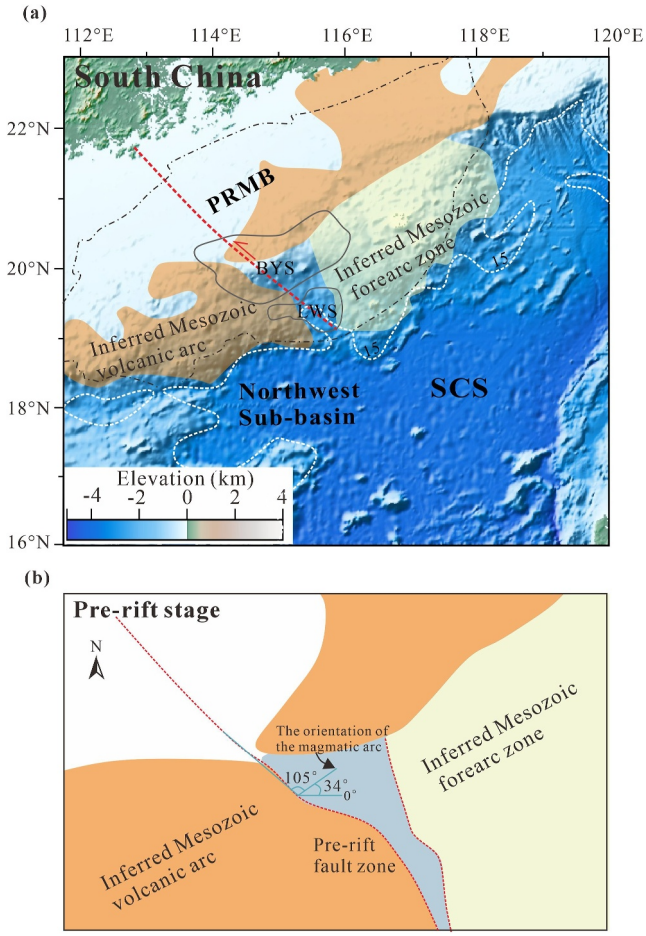

Figure 2. (a) Location of the Mesozoic volcanic arc (orange) and forearc basin (sand color) in the northern South China Sea (SCS) (Li et al., 2018; Zhao et al., 2019). The red dashed line represents the inferred NNW-trending Mesozoic fault, identified from gravity data (Chen et al., 2005), extending through the Baiyun and Liwan Sag. The white dashed line marks the 15 km contour of the crust thickness. PRMB, Pearl River Mouth Basin. SCS, South China Sea. BYS, Baiyun Sag. LWS, Liwan Sag. (b) Schematic map showing the pre-rift fault zone between the Mesozoic volcanic arc and forearc basin in the northern SCS, modified from Zhao et al. (2019).

(Li et al., 2018; J. Y. Zhang, Zhao, Sun, et al., 2023; Zhao et al., 2019). A recent study based on a 3D tomographic P-wave velocity model (J. Z. Zhang, Zhao, Ding, et al., 2023) supports the idea that inherited lithospheric heterogeneities caused by Mesozoic magmatic intrusions may have led to the different opening styles of the SCS. Additionally, a 2D thermo-mechanical model suggests that variation in the subduction duration of the paleo-SCS could be a contributing factor to the different breakup locus (arc/forearc) in the northwestern and northeastern margins (F. C. Li, Wu, et al., 2020). Neither the aforementioned tomography (J. Z. Zhang, Zhao, Ding, et al., 2023) nor the 2D numerical modeling (F. C. Li, Wu, et al., 2020) were able to study how the heterogeneities exerted control on the segmentation of the northern margin of the SCS.

In addition, geophysical data indicate the presence of a Mesozoic NNW–SSE pre-rift fault zone between the northeastern and northwestern segments (Figures 2a and 2b) (Chen et al., 2005; Li et al., 2018; Yan et al., 2014; Zhao et al., 2019), potentially acting as a transfer fault zone that accommodated intraplate strain during the differential evolution of the northern SCS (J. Z. Zhang, Zhao, Ding, et al., 2023; Zhao et al., 2019). However, detailed research on how this pre-existing fault zone accommodated the differential deformation between the northeastern and northwestern segments during Cenozoic is lacking.

To better constrain the role of inherited lithospheric structures in shaping rift segmentation, we employ an integrated approach combining 3D analog modeling with 2D thermo-mechanical numerical simulations. The analog models adopt a four-layer configuration representing the brittle upper crust, ductile lower crust, lithospheric mantle, and asthenosphere. These experiments are designed to simulate the effects of lithospheric heterogeneity, introduced by Mesozoic magmatic activity and a pre-existing NWW-trending fault zone, on the segmentation characteristics of the northwestern and northeastern margins of the SCS. The complementary numerical models incorporate inherited rheological variations and are capable of capturing thermal structures while avoiding boundary effects that cannot be fully addressed in analog setups. This combined modeling framework enables a systematic investigation of how pre-existing structural and rheological heterogeneities influence rift evolution and segmentation along the SCS margin. The new insight provided by this study not only enhances our understanding of the SCS but also contributes to a broader comprehension of complex 3D tectonic processes in passive continental margins.

2. Tectonic Setting

2.1. Geological Evolution

The SCS is the largest marginal sea in the western Pacific region, trending NE-SW and is bounded by China to the north, Vietnam to the west, the Philippines to the east and Borneo to the south (Figure 1a). The prolonged subduction of the paleo-Pacific since the Triassic resulted in widespread magmatism along a broad belt in South China (Li et al., 2018; Savva et al., 2014; Wang et al., 2012). Previous studies suggest that distinct ENE-trending Mesozoic magmatic products developed beneath the syn-rift basins of the northern SCS (Cheng et al., 2021; Li et al., 2018; Shao et al., 2017; Yan et al., 2014; Zhou et al., 2008). A remarkable high magnetic anomaly belt along the northern SCS margin is interpreted as a remnant of a Mesozoic subduction arc (Han et al., 2016; Li et al., 2018; Yan et al., 2014). Integrating reprocessed magnetic data with petrological evidence, Li et al. (2018) propose that a major magmatic body identified onshore extends laterally for 60 km beneath the margin at depths of 18–24 km and is the expression of paleo-Pacific subduction-related magmatism.

The opening of the SCS results from the southeastward subduction of a proto-oceanic plate, commonly referred to as the proto SCS (proto-SCS), beneath Borneo (Hall, 2002; F. C. Li, Wu, et al., 2020; Mazur et al., 2012; Wu & Suppe, 2018). Some researchers have proposed the proto-SCS to be a backarc extensional basin associated with the continued subduction retreat of the paleo-Pacific slab during the Late Cretaceous (e.g., Bai et al., 2015; Morley, 2012; Zahirovic et al., 2014). Tectonic reconstructions suggest that the proto-SCS subduction initially began along the South China margin and later switched to southeastern direction in the Eocene (∼45 Ma) (Hall, 2002; Wu & Suppe, 2018). This southeastward subduction induced tectonic extension on the South China margin, leading to the rifting and drifting of several continental blocks during the Eocene, which ultimately resulted in seafloor spreading of the present-day SCS between ∼33 and ∼15 Ma (Li et al., 2014, 2015; Mazur et al., 2012).

Geophysical data indicate that pre-existing crustal heterogeneities, such as Mesozoic magmatic intrusions with different rheological properties, have long been considered key structural controls on the evolution of the SCS rifted margin (Li et al., 2018, 2019; Sun et al., 2016; Yan et al., 2014; J. Y. Zhang, Zhao, Sun, et al., 2023; Zhao et al., 2019). Rifting likely initiated along the onshore Mesozoic magmatic zone, emplaced by paleo-Pacific subduction (Li et al., 2018, 2019; Sun et al., 2016; Yan et al., 2014; J. Y. Zhang, Zhao, Sun, et al., 2023; Zhao et al., 2019). This zone may have been mechanically weak due to the inherent heat and melt (Han et al., 2016; Li et al., 2018; Yan et al., 2014), processes known to reduce lithospheric strength (Kusznir & Park, 1987). Additionally, ongoing magmatism driven by corner flow, associated with the northwestward subduction of the proto-SCS before approximately 45 Ma ago, may have further contributed to the weakening (Hall, 2002; F. C. Li, Wu, et al., 2020; Wu & Suppe, 2018). The oldest rock cores from the northeastern forearc basin zone reveal substantial Mesozoic sedimentary deposits, with the earliest strata potentially dating to the Triassic (Shao et al., 2007; Wu et al., 2007; Yan et al., 2014).

The northern continental margin of the SCS exhibits low lithospheric strength (Shi et al., 2005; Yang et al., 2022; Zhang & Wang, 2000; Zhang & Xiong, 2001; Zhao et al., 2018). Forward and inverse basin modeling results (Clift et al., 2015; Tong et al., 2009) indicate that the formation of the northern margin was influenced by weak lower crust, which led to pronounced depth-dependent deformation and thinning during rifting (Ding et al., 2013; Zhao et al., 2018). The lower crust in this region exhibits relatively high viscosity, estimated to range from 10^{21} to10^{22} Pa·s (Clift et al., 2002) or 10^{21}–10^{23} Pa·s (Zhang & Xiong, 2001), approximately two orders of magnitude higher than that of the lithospheric mantle (10^{20}–10^{21} Pa·s) (Zhang & Wang, 2000; Zhang & Xiong, 2001). Previous studies suggest that the initial crustal thickness may have been comparable to the present-day average of ∼35 km in the southernmost part of China (Clift & Sun, 2006; Deng et al., 2020; Li et al., 2019). The vertical density structure of the crust, derived from joint inversion of gravity, magnetic, and seismic data shows that the upper crust is slightly thicker than the lower crust on the continental shelf of the SCS (Ren et al., 2018). The full spreading rate in the eastern sub-basin varies from 20 to 80 mm/yr, generally decreasing over time, except in the period between 26.0 Ma and a ridge jump at 23.6 Ma, during which the rate was the lagest (70 mm/yr on average; Li et al., 2014).

2.2. Along-Strike Differences in Deformation Style of the Northern SCS

The northern SCS exhibits along-strike variation in deformation patterns of the continental crust (Hayes & Nissen, 2005; Franke et al., 2014; Zhao et al., 2019; J. Z. Zhang, Zhao, Ding, et al., 2023). The northwestern segment shows fault-controlled thinning driven by detachment faults (Huang et al., 2021; Yang et al., 2018; J. Z. Zhang, Zhao, Ding, et al., 2023). A series of tilted fault blocks caused by detachment faults is blanketed by thick sedimentary cover (Hayes & Nissen, 2005; Savva et al., 2014; Yang et al., 2018; Zhao et al., 2019). Unlike magma-poor passive continental margins that exhibit mantle exhumation, rock samples from International Ocean Discovery Program (IODP) Expeditions 367/368/368X indicate a rapid transition from continent to ocean in northwestern segment, with no evidence of mantle exhumation (Childress et al., 2020; Deng et al., 2020; Larsen et al., 2018; Stock et al., 2018; Sun et al., 2018). Instead, based on high-resolution seismic data, Deng et al. (2020) suggest that the thermal and mechanical weakening of this broad continental domain allowed for the formation of metamorphic core complexes, boudinage of the upper crust and exhumation of middle/lower crust through detachment faulting.

The crustal thickness decreases sharply from north to south, characterized by a wide continental shelf, a narrow and steep slope, and a distal domain with extremely thin crust (Savva et al., 2014; Yang et al., 2018) (Figure 1b).

As shown in Figure 1a, 3D gravity inversion results indicate that both the highly extended continental crust (<15 km crustal thickness) and the moderately extended continental crust (15–20 km crustal thickness) are relatively narrow in the northwestern segment (Li et al., 2019).

In contrast, tectonic deformation in the northeastern segment is less abrupt and more broadly distributed (Figure 1c) (J. Z. Zhang, Zhao, Ding, et al., 2023). This segment is also characterized by the presence of a high-velocity lower crust (HVLC) layer (McIntosh et al., 2014; Wang et al., 2006; Yan et al., 2001; J. Y. Zhang, Zhao, Sun, et al., 2023; J. Z. Zhang, Zhao, Ding, et al., 2023; Zhao et al., 2019). However, key features typical of magma-rich margins, such as seaward dipping reflector sequences (SDRs) have not yet been reported. A pseudo-3D velocity model of the northeastern SCS, derived from integration and interpolation of 12 2D P-wave velocity models, suggests that the HVLC in the northeastern margin is associated with magmatic intrusions caused by asthenospheric decompression melting during the post-rift stage (Cheng et al., 2021). Additionally, the lower continental slope of the northeastern segment exhibits more faults compared to the northwestern segment (Zhao et al., 2019). These previous studies show that both the ultra-thinned (crustal thickness less than 15 km, Figure 1a) and the moderate extended continental crust zone (15–20 km, Figure 1a) in the northeast are wider than that in the northwest (Figure 1a) (Bai et al., 2019; Li et al., 2019; Pichot et al., 2014; Tsai et al., 2004).

A narrow boundary zone, approximately coincident with the Baiyun and Liwan Sags, separates the northeastern and northwestern segments (Figure 2b) (J. Z. Zhang, Zhao, Ding, et al., 2023; Zhao et al., 2019). Gravity and magnetic anomaly data reveal several NNW-trending left-lateral strike-slip fault zones along the northern margin of the SCS, one of which extends directly through the Baiyun and Liwan Sags (Chen et al., 2005; Figure 2a). Seismic profile analysis and analog modeling suggested that the fault development in the Baiyun Sag was controlled by both the regional extensional stress field and the NW-trending basement faults (Sun et al., 2005). Geophysical data further indicate that the Baiyun and Liwan Sags likely formed along a NNW pre-rift fault zone that experienced significant thinning before Cenozoic continental rifting (Zhao et al., 2019). This pre-existing structure induced lateral rheological variations, influencing continental margin geometry and deformation during Cenozoic rifting.

The northern SCS rifted margin is neither a typical magma-poor nor a typical magma-rich margin, exhibiting distinct structural segmentation that incorporates elements of both end-member margin types. Previous studies have primarily attributed this segmentation to the influence of Mesozoic magmatic activity (Li et al., 2018, 2019; Shao et al., 2017; Yan et al., 2014; J. Z. Zhang, Zhao, Ding, et al., 2023; Zhao et al., 2019). However, the differential evolution of the northern SCS margin and the role of pre-existing faults between the northwestern and the northeastern segments are not yet fully understood.

3. Analog Modeling

In this section, five analog models with different initial conditions were designed to investigate the control exerted by magmatic heterogeneity on the segmentation along the northern margin of the SCS.

3.1. Experimental Setup and Configurations

The models were built within a transparent plexiglass sandbox with internal dimensions of 40 × 30 × 25 cm (Figure 3a). A mobile plexiglass wall was placed vertically into the sandbox and pulled at a constant rate of 0.024 mm/s by a motor (Figure 3a). Based on P-wave seismic velocity (Vp) models from the northern SCS margin obtained by IODP Expeditions 367/368/368X (Zhang, Zhao, Ding, et al., 2023), and previous numerical and analog models simulating the opening of the SCS (Ding & Li, 2016; F. C. Li et al., 2019, 2020, 2021), our scaled 3D experiments consist of three distinct compositional lithospheric layers, representing the brittle upper crust, ductile lower crust, and ductile lithospheric mantle (Figures 3a and 3b). To simulate the gradual increase in density and decrease in viscosity from shallow to deep within the SCS lithosphere, we proportionally mixed common experimental materials.

Three types of Polydimethylsiloxane (PDMS) with different strengths were used (density and viscosity values are listed in the footnote of Table 1). The PDMS mixture analog material exhibits slightly non-Newtonian behavior. A 1-cm thick layer of plastic powder (PVC) (density 960 kg/m^3) with Mohr-Coulomb behavior (e.g., Graveleau et al., 2011; Mao et al., 2021) simulated the brittle upper crust, possessing an internal friction angle of 34° and a cohesion of 36 Pa. A 0.75-cm thick layer composed of a PDMS1- corundum mixture (density 1,150 kg/m^3,

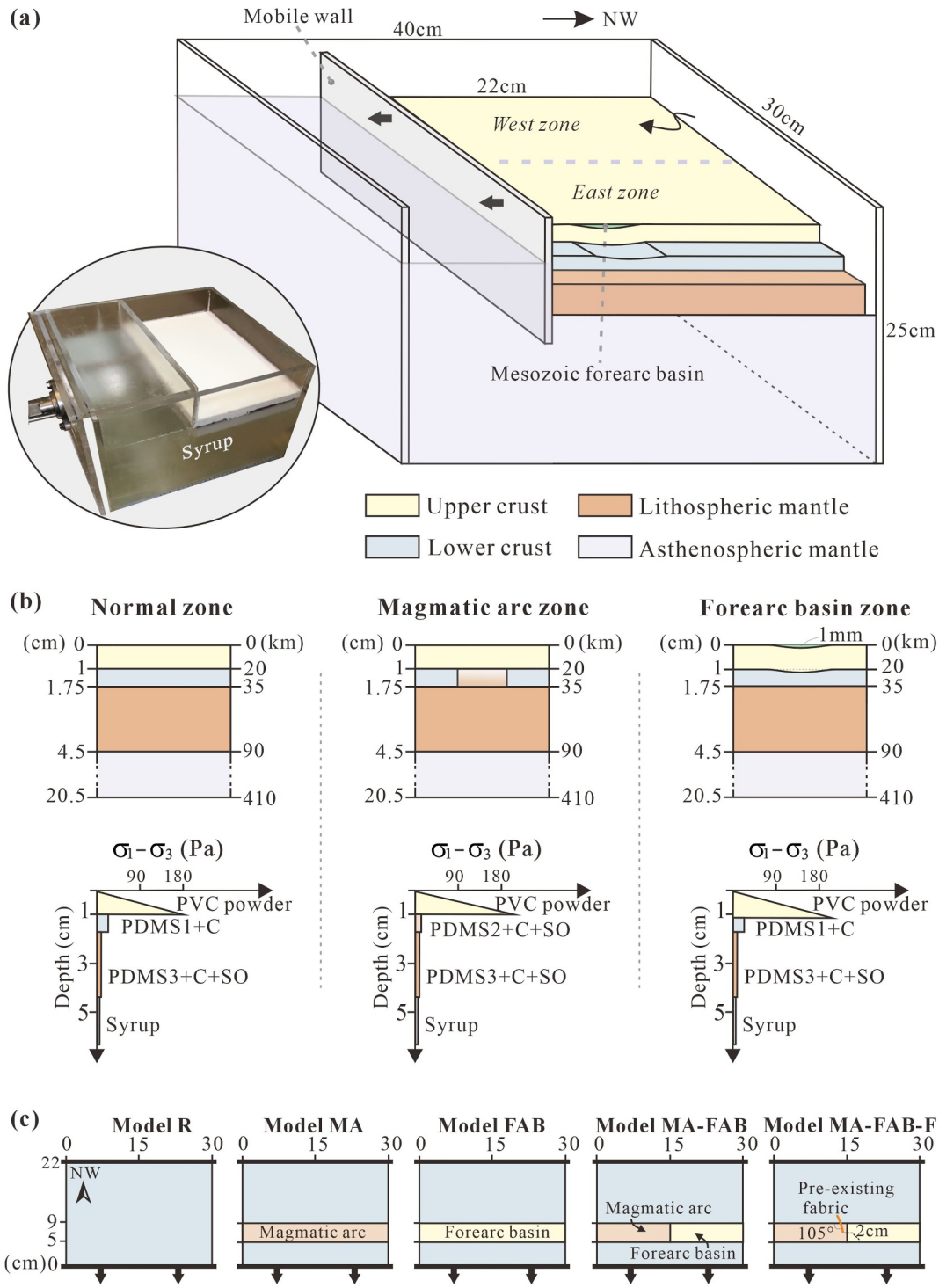

Figure 3. Model set-up. (a) Deformation apparatus and scheme showing the initial lithospheric setting. (b) Schematic cross sections illustrating the initial rheological layering for each segment and strength profiles. For brittle layers (upper crust), the strength profiles are calculated using the equation from Brun (2002): $(\sigma_1 - \sigma_3)_{\text{brittle}} = 2\rho_b g h_b$, where g is the acceleration due to gravity (9.81 m/s^2) and ρ_b and h_b are the density and thickness of the brittle layer, respectively. For ductile layers (lower crust), the strength is given by: $(\sigma_1 - \sigma_3)^n{}_{\text{viscous}} = \eta\dot{\varepsilon}$, where η is the viscosity, $\dot{\varepsilon}$ is the strain rate ($\dot{\varepsilon}$ = velocity/length) and n is the power-law exponent of the material (Brun, 2002). The PDMS-based mixture used as an analog material is slightly non-Newtonian (Molnar et al., 2017), with a power-law exponent $n \sim 1.2$. (c) Top view of the experimental models under different initial conditions. PDMS, Polydimethylsiloxane. C, corundum. SO, silicone oil.

Table 1
Characteristics of Experimental Materials and Scaling of Models

Layer material		Thickness (m)		Density (kg/m^3)		Viscosity (Pa·s)	
		Model	Nature	Model	Nature	Model	Nature
Brittle upper crust							
Forearc basin zone Magmatic arc zone	PVC	1.1×10^{-2}	2.2×10^{4}	960	2,400	–	–
	PVC	1×10^{-2}	2×10^{4}	960	2400[a]	–	–
Ductile lower crust							
Normal lower crust	PDMS1+C (1:0.3)	6.5×10^{-3}	1.3×10^{4}	1,156	2870[b]	7.15×10^{4}	10^{22}
Magmatic arc	PDMS2+C + SO (1:0.5:0.2)	7.5×10^{-3}	1.5×10^{4}	1,200	3,010	1×10^{4}	10^{21}[c]
Lithospheric mantle	PDMS3+C + SO (1:0.7:0.4)	2.75×10^{-3}	5.5×10^{4}	1,250	3,125	4.3×10^{3}	6×10^{20}
Asthenosphere	Syrup	1.6×10^{-1}	3.2×10^{5}	1,400	3,383	304	10^{19}

Note. PDMS1, the density and viscosity are 913 kg/m^3 and 5.6×10^4 Pa·s, respectively; PDMS2, the density and viscosity are 898 kg/m^3, 1.75×10^4 Pa·s, respectively; PDMS3, the density and viscosity are 876 kg/m^3, 1.18×10^4 Pa·s, respectively. PVC, plastic powder. PDMS, Polydimethylsiloxane. C, corundum. SO, silicone oil. [a]Liu et al. (2015). [b]H. L. Li et al. (2020). [c]Clift et al. (2002).

viscosity 71,520 Pa·s) simulated the ductile lower crust. The weak magmatic arc in the northwestern margin was simulated by a mixture of corundum-PDMS2-silicone oil with a density of 1,200 kg/m^3 and a viscosity of 10,000 Pa·s. A 2.75-cm thick layer of PDMS3-corundum-silicone oil mixture (density 1,250 kg/m^3, viscosity 4,300 Pa·s) was used to simulate the low-strength lithospheric mantle (Figure 3b). The 4.5-cm thick model lithosphere was isostatically supported by a lower viscosity (Figure 3b), higher density model asthenosphere, simulated by a 16-cm thick syrup layer (density 1,400 kg/m^3, viscosity 304 Pa·s).

A lateral pre-existing heterogeneity was set up in the models, based on structural information from previous studies on the northern continental margin of the SCS (Li et al., 2018; Yan et al., 2014; J. Y. Zhang, Zhao, Sun, et al., 2023; J. Z. Zhang, Zhao, Ding, et al., 2023; Zhao et al., 2019) (Figure 3c). Following Li et al. (2018), who identified the remnant Mesozoic magmatic arc at depths of 18–24 km, we placed a 4-cm wide linear weak zone in the lower crustal part of the model to represent the ENE-trending Mesozoic magmatic arc (Figures 3b and 3c). The magmatic arc material in our experiments has higher density due to its mantle origin (Han et al., 2016; Li et al., 2018; Yan et al., 2014) and lower viscosity to reflect its weaker nature relative to the normal lower crust (Han et al., 2016; Li et al., 2018; J. Y. Zhang, Zhao, Sun, et al., 2023; J. Z. Zhang, Zhao, Ding, et al., 2023; Zhao et al., 2019) (Table 1). Forearc basins are typically characterized by thick abyssal and shallow marine sediments (Frisch et al., 2011), predominantly deposited on an accretionary complex basement (Dickinson, 1995). The northern margin of the SCS is no exception (Suo et al., 2019), which is why we placed a thicker brittle layer representing Mesozoic sediments in the forearc basin zone. PVC, with the same properties used to represent the brittle crust, was used to approximate the Mesozoic sediments (Figures 3a and 3b). Referring to the kinematic reconstructions of the Mesozoic evolution of the Southeast China continental margin (Suo et al., 2019; their Figure 16), we assigned a slightly thinner lower crust to the forearc basin zone in our model compared to the normal lower crust (Figure 3b).

Figure 3c shows the initial lower crustal conditions in the model setups. The zones representing the magmatic arc and the forearc basin in models are simplified as MAZ and FBZ, respectively. Model R serves as a reference model, simulating extension process without any lateral heterogeneity. Model MA and Model FAB are designed as single-factor experiments to simulate extension in the presence of lithospheric heterogeneity induced by a magmatic arc and a forearc basin, respectively. Model MA-FAB simulates extension with a magmatic arc in the northwestern segment and a forearc basin in the northeastern segment. Model MA-FAB-F follows the same setup as Model MA-FAB, but includes an additional lithospheric-scale, pre-existing NNW-oriented fault zone that separates the northeastern and northwestern segments (Figure 3c).

Referring to previous works (Bellahsen & Daniel, 2005; Corti et al., 2007), the pre-existing NNW-trending lithospheric-scale strike-slip fault zone (Chen et al., 2005; Sun et al., 2005; Zhao et al., 2019) (Figure 2b) is represented in the model by a 0.1-cm-thick, 3-cm-wide, nearly vertical piece of cardboard cutting through the sand layer down to the top of the syrup. The orientation of the cardboard piece (Figure 3c) is based on the

observed angular relationship (105°) between the pre-existing NNW-trending main fault and the ENE-trending magmatic heterogeneity (Figure 2b). Its length is determined by the natural spatial relationship between pre-existing NNW-trending faults and the magmatic heterogeneity (Figure 2a). Geophysical data indicate that this pre-existing fault terminates at the southern boundary of the magmatic heterogeneity (Figure 2a) (Chen et al., 2005; Zhao et al., 2019). We hypothesize that the breakup of the SCS was focused at the center of the magmatic arc and forearc basin, as geological evidence suggests rifting initially began within these regions (Figure 2) (Li et al., 2018; J. Y. Zhang, Zhao, Sun, et al., 2023; Zhao et al., 2019). This further implies that before rifting, the pre-existing NNW-trending main fault terminates at the center of the magmatic heterogeneity. Therefore, at the initial stage of the experiment, the cardboard piece representing this pre-existing fabric occupies half (2 cm) of the weak zone's total width and extends an additional 1 cm northward beyond it (Figure 3c).

During the experiment, the model was subjected to total extension by 60 mm at a constant velocity of 0.024 mm/s. The extension direction was perpendicular to the pre-existing magmatic arc and forearc basin. The model evolution was recorded by top- and side-view photographs taken at regular time intervals (2 min). Additionally, a 3D scanner (resolution is 0.02 mm) was employed to scan the model's surface every 2 cm of extension, providing quantitative surface elevation data for analysis.

3.2. Model Scaling

Three similarity criteria (geometric, kinematic, and dynamic) ensure proper model scaling (Hubbert, 1937). According to the length ratio ($l_{m/n} = 5 \times 10^{-7}$, where m and n refer to model and real length, respectively), our experimental lithosphere thickness of 1 cm corresponds to 20 km in nature (Figure 3b). This implies a value of 4.5 cm, consistent with the observed lithospheric thickness (~90 km) on the continental margin of the SCS (Kato & Jordan, 1999). The crustal thickness of 35 km (Clift & Sun, 2006; Deng et al., 2020; Hayes & Nissen, 2005; Li et al., 2019) is scaled down to 1.75 cm in the models (Figure 3c). All experiments were carried out under normal gravity conditions (9.8 m/s^2), resulting in a gravity scale ratio of $g_{m/n} = 1$. Gravity inversion suggests that the density at the top of the lower crust is approximately 2,870 kg/m^3 in the northern SCS (H. L. Li et al., 2020Li, Wu, et al., 2020). A lower crustal density of $\rho_n \approx 2{,}870$ kg/m^3 is represented by a model density of $\rho_m \approx 1{,}156$ kg/m^3, leading to a density scaling factor of $\rho_{m/n} = \rho_m/\rho_n = 0.4$. The stress ratio is calculated as $\sigma_{m/n} = \rho_{m/n} g_{m/n} l_{m/n} = 2 \times 10^{-7}$. The viscosity scaling is: $\eta_{m/n} = \eta_m/\eta_n = 7.15 \times 10^{-18}$, where the model's normal lower crustal viscosity (silicone) of 7.15×10^4 Pa·s represents 10^{22} Pa·s in nature, aligning with previous estimates (10^{23}–10^{21} Pa·s) (Clift et al., 2002; Zhang & Xiong, 2001). Kinematic similarity was achieved by calculating the strain rate ratio $\varepsilon_{m/n}$, derived from stress ratio $\sigma_{m/n}$ and viscosity ratio $\eta_{m/n}$ (Weijermars & Schmeling, 1986): $\varepsilon_{m/n} = \sigma_{m/n}/\eta_{m/n} = 2.8 \times 10^{10}$. The velocity ratio $v_{m/n}$ is determined as: $v_{m/n} = \varepsilon_{m/n} l_{m/n} = 2.8 \times 10^{10} \times 5 \times 10^{-7} = 1.4 \times 10^4$. Thus, the reference velocity of 0.024 mm/s scale to ~5 cm/yr in nature. The material properties and scaling parameters of the models are summarized in Table 1.

3.3. Simplifications and Limitations of Analog Modeling

Our analog models inherently involve several simplifications and limitations: (a) The experiments are based on the principle of similarity, which involves scaling the geometric, kinematic, and dynamic parameters of natural systems in proportion. (b) The rheological behavior of the lithosphere is simplified. Analog materials typically exhibit idealized brittle or viscous behavior, while natural lithospheric materials display temperature-dependent, non-Newtonian, and composite rheology that are difficult to reproduce in the laboratory. (c) Continental rifting is a thermomechanical process that depends on temperature and composition of the lithosphere (e.g., Corti, 2004; Petersen & Schiffer, 2016). The primary limitations of the present modeling stem from the rheology of the experimental materials. Certain thermal effects, such as crystallization-melting, variations in magma rheology, and thermal weakening of the country rocks, cannot be simulated. Therefore, continental extension is simplified as a purely mechanical process in our experiments. (d) Although isostatic compensation provided by the asthenosphere is considered, thermal adjustments of lower crustal viscosity and low-strength lithospheric mantle during deformation are not incorporated. As in previous studies (Calignano et al., 2017; Corti et al., 2007; Molnar et al., 2017, 2020; Nestola et al., 2015; Santimano & Pysklywec, 2020; Sokoutis & Willingshofer, 2011; Zwaan & Schreurs, 2023), some thermal effects are approximated through depth-dependent strength variations in the models. (e) The initial model setup (Figure 3c) assumes that the weak magmatic arc had not fully cooled before the breakup of the SCS. However, our experiments do not account for post-rift magma intrusion (Liu et al., 2015; Shi et al., 2005), nor the HVLC potentially associated with magmatic underplating or intrusion (Cheng

et al., 2021). (f) Additionally, transient thermal changes during model development cannot be simulated. (g) Furthermore, this study primarily focuses on the passive extension phase preceding ~33 Ma, without considering the effects of seafloor spreading (~33–15 Ma) (Li et al., 2014, 2015) or subsequent thermal subsidence.

Despite these simplifications, as discussed in previous analog modeling studies (Corti, 2004; Molnar et al., 2017, 2020; Zwaan & Schreurs, 2023), we consider the present model valid for the specific scenarios investigated, namely the impact of pre-existing Mesozoic heterogeneity on differential thinning of the northern SCS.

3.4. Analog Modeling Results

This section presents the evolution process captured by the camera (Figure 4) and the corresponding digital elevation models (DEMs) (Figure 5) from five experiments, where the DEMs provide a direct visualization of crustal thinning features. Additionally, we statistically analyze the variation in fault numbers (Figures 6a–6e) and width of the northern margin (defined as the secondary thinning zone, which lies between the main northern boundary fault and the northern boundary of the central fault zone) (Figures 6f–6j). To quantify these variations, we measure fault number and secondary thinning width along three reference lines (Figure 6a): one at the center of the experiment (L2) and the other two positioned 6 cm to the left (L1) and right (L3). This approach is applied consistently across all experiments to ensure comparability. These analyses provide a quantitative assessment of tectonic evolution under different initial conditions.

1. Model R (reference model with homogeneous lithosphere)
   Model R simulates rifting of a homogeneous reference lithosphere. During the initial 2 cm of extension, fault development is minimal, with thinning occurring only near the moving wall (Figures 4a and 5a, 20 mm extension), which can be attributed to boundary effect. As the extension increases (Figure 4a, 40 mm extension), deformation propagates and leads to the development of a series of discontinuous faults with small displacements (Figure 5a; 40 mm extension), forming a distributed rift zone. Upon completion of the extension (Figure 4a, 60 mm extension), as displacements continue to increase, the number of faults also increases significantly (Figure 6a), and the main rift zone widens (Figure 5a, 60 mm extension). Stress propagates toward the fixed wall, generating faults similar to those in the main rift zone, though with fewer faults and larger spacing (Figures 4a and 5a; 60 mm extension).
   Due to the lateral homogeneity of the lithosphere, fault displacements, fault number, and main deformation zone width remain consistent from west to east, except for the boundary effects at both sides of the model. Ultimately, the main deformation zone exhibits distributed deformation with uniform thinning along the rift axis.
2. Model MA (crustal heterogeneities in the form of a magmatic arc)
   Model MA simulates rifting in the presence of a pre-existing weakness zone, representing a weak magmatic arc in the lower crust. During the initial extension stage (Figures 4b and 5b, 20 mm extension), deformation localizes along the pre-existing weakness zone, forming continuous boundary faults perpendicular to the extension direction. Within the rift zone, two parallel sub-grabens develop, and the overall rift exhibits an alternating horst and graben pattern (Figure 5b, 20 mm extension). At the westernmost and easternmost ends of the rift zone, faults are relatively dense due to boundary effects, but the fault displacements are smaller (Figure 5b, 20 mm extension).
   With further extension (Figures 4b and 5b, 40 mm extension), deformation becomes increasingly focused in the rift center, where the original central horst undergoes further dissection and thinning, forming a broad and complex depression (Figure 5b, 40 mm extension). The boundary subbasins (secondary thinning zones) formed on both sides of the rift zone do not widen significantly. The northern secondary thinning zone near L2 (Figure 4b) exhibits a slight increase in width (Figure 6g), while the boundaries on both sides slightly narrow (Figure 6g). At the end of the extension (Figure 5b, 60 mm extension), a deep, wide, and complex basin forms. Remnants of early-stage ridges that were not fully cut through persist as small uplifts. Faults within the rift zone are discontinuous and short. The boundary subbasins become narrower compared to the initial stage due to outward propagation of the central faults (Figure 6g).
   Throughout the extension phase (Figure 5b), the degree of thinning remains generally uniform along the rift axis, and the structural style is consistent, except at the rift ends where boundary effects are observed. Consequently, the fault number increases with extension, but fault distribution remains relatively uniform along strike (from L1 to L3) at each stage (Figure 6b).

10.1029/2024TC008541

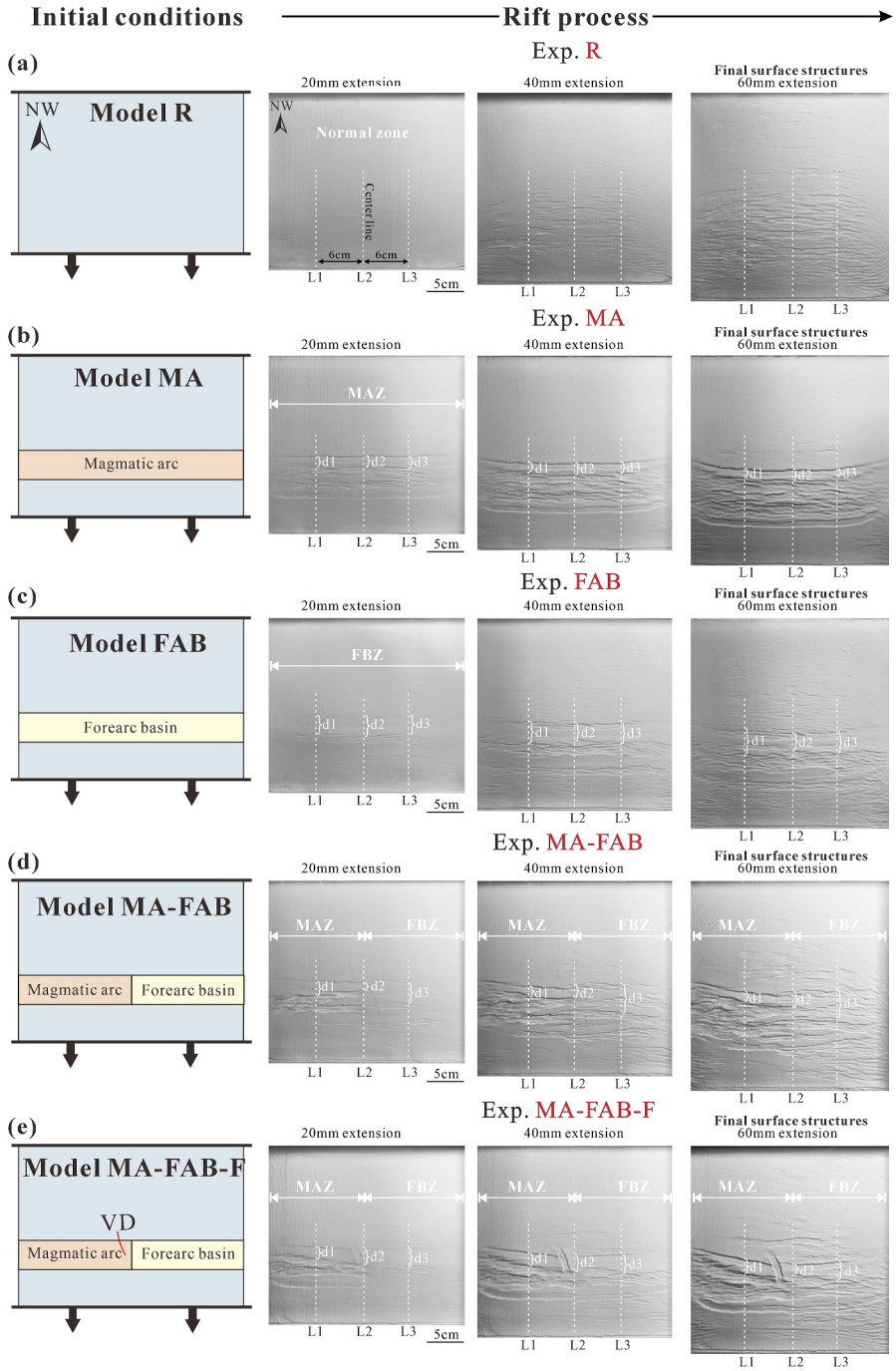

Figure 4. Initial boundary conditions (left panel) and the experimental evolution process recorded by the camera at 20 mm, 40 mm, and 60 mm extension (left to right). The rifting evolution of Model R (panel a), Model MA (panel b), Model FAB (panel c), Model MA-FAB (panel d), and Model MA-FAB-F (panel e) is shown. Black arrows indicate the extension direction. MAZ, magmatic arc zone. FBZ, forearc basin zone. L1, L2, and L3 mark the western, central, and eastern segments, respectively, where fault statistics were conducted, considering only faults that cross these lines. d1, d2, and d3 denote the widths of the secondary thinning zones at L1, L2, and L3, respectively.

3. Model FAB (crustal heterogeneities in the form of a forearc basin)

   Model FAB is designed to simulate the influence of pre-existing forearc basins on the rift continental margin (Figure 3c). During the early extension stage (Figure 4c, 20 mm extension), two continuous, elongated sub-basins develop on both sides of the rift zone. Unlike the fault-controlled boundary subbasins in Model MA

10.1029/2024TC008541

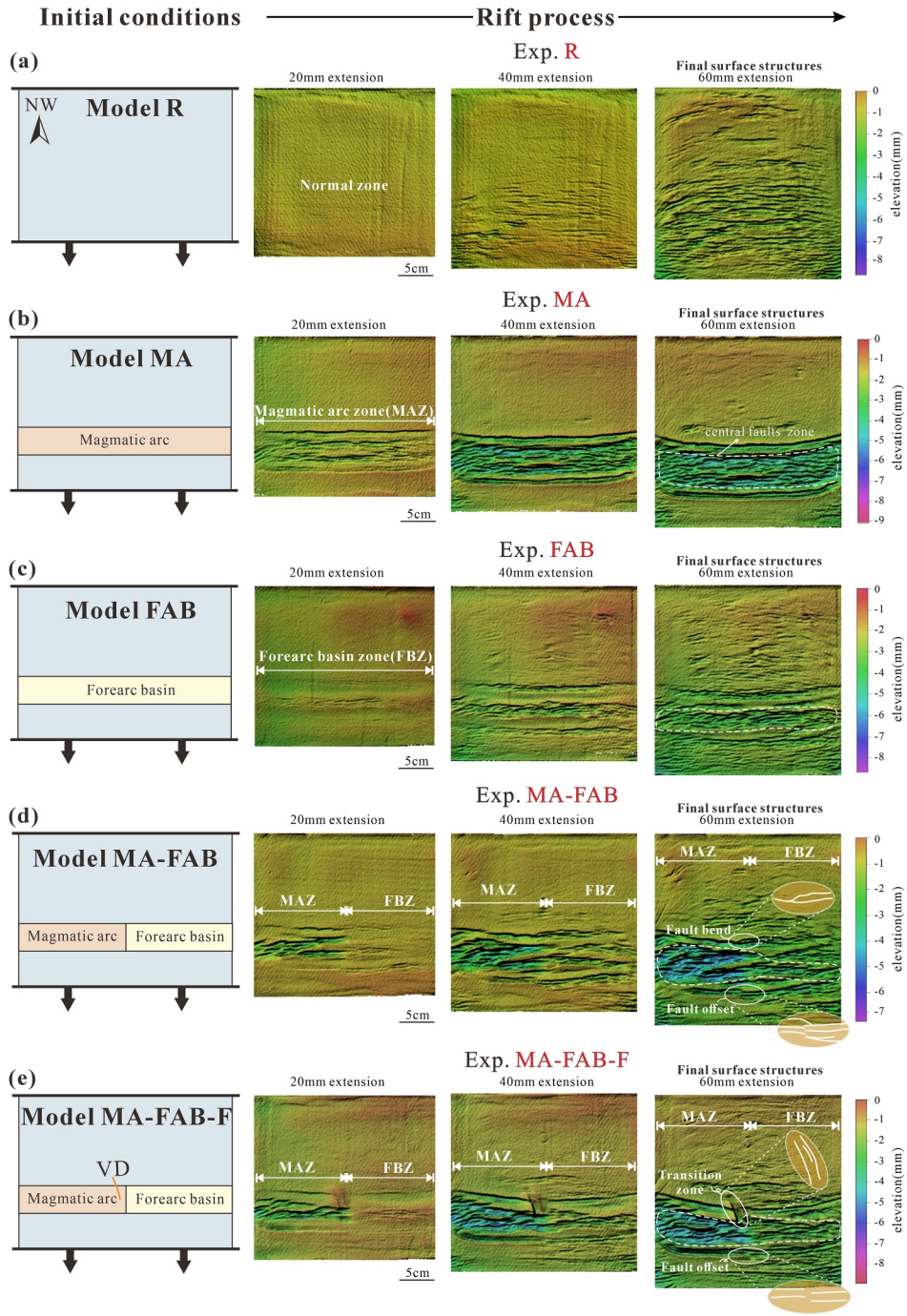

Figure 5. Initial boundary conditions of each model (left panel) and related top-view digital elevation models (DEMs) showing the experimental evolution process at 20 , 40 and 60 mm extension (left to right). DEMs illustrate the model surface for Model R (panel a), Model MA (panel b), Model FAB (panel c), Model MA-FAB (panel d), and Model MA-FAB-F (panel e). The black arrows represent the extension direction. MAZ, magmatic arc zone. FBZ, Forearc basin zone. The orange dashed line represents the inferred central fault zone, estimated based on fault locations and relative elevation variations in the DEMs.

(Figures 4b and 5b, 20 mm extension), these subbasins in Model FAB are primarily characterized by subsidence, without boundary faults developing at this stage (Figure 5c, 20 mm extension). The central rift zone is dominated by small, dense faults, with minimal subsidence, creating a topography where the rift zone is elevated in the center and subdued on the sides (Figure 5c, 20 mm extension).

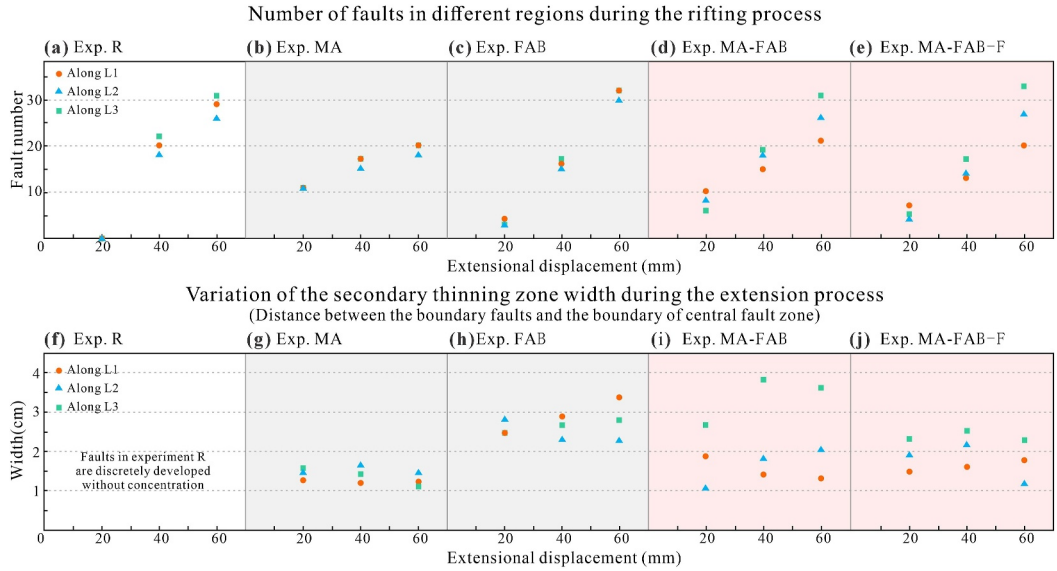

Figure 6. Quantitative analysis of fault number and secondary thinning zone width during the rifting process. (a–e) Variation in fault number across different zones throughout rifting. (f–j) Evolution of secondary thinning zone width in different regions. The secondary thinning zone width is measured as the distance between the main boundary fault and the boundary of the central fault zone. To ensure experimental comparability, measurements were taken at consistent locations across all stages of the experiments.

As extension progresses (Figures 4c and 5c, 40 mm extension), the central fault zone widens and deepens (Figure 5c, 40 mm extension), accompanied by an increase in fault numbers (Figure 6c). The boundary fault zones develop along the early-formed boundary subsidence zones, creating a separation from the central fault zone, resulting in distributed rift deformation (Figures 4c and 5c, 40 mm extension). At the end of extension (Figure 5c, 60 mm extension), deformation is less concentrated along the forearc basin than in Model MA. Instead, it is more widely distributed, extending beyond the forearc basin. Throughout the different stages of extension, the secondary thinning zone in Model FAB is generally wider than that in Model MA. In contrast to Model MA, where the secondary thinning zone slightly narrows (Figure 6h), it undergoes progressive widening with increasing extension in Model FAB. However, near L2 (Figure 4b), where the secondary thinning zone is intersected by the propagating central faults, a slight width reduction is observed (Figure 6h). Overall, in Model FAB, deformation is more distributed, and the degree of crustal deformation (Figure 5c, 60 mm extension) is less pronounced than in Model MA (Figure 5b, 60 mm extension).

4. Model MA-FAB (along-strike crustal heterogeneities with magmatic arc and forearc basin)

Imposing a variable lithosphere strength in Model MA-FAB (composition and thickness) simulates the magmatic arc in the northwestern segment and the forearc basin in the northeastern segments of the northern SCS margin (Figure 3b).

The evolutionary processes of the MAZ and FBZ in Model MA-FAB are similar to those observed in Model MA (Figure 5b) and Model FAB (Figure 5c), respectively, ultimately leading to distinct segmentation characteristics. In the MAZ, the central depression deepens and widens, with a sharp shallowing toward the boundaries (Figure 5d, 60 mm extension). In contrast, thinning in the FBZ is more gradual. Over time, deformation in the FBZ expands significantly compared to the MAZ. At the MAZ-FBZ junction, boundary faults bend or develop offsets (Figure 5d, 60 mm extension). The central fault zone in this junction is segmented by an uplift extending into the FBZ, forming an alternating uplift-subbasin structural pattern (Figure 5d, 60 mm extension). Consequently, the central fault zone in the FBZ is relatively narrow (Figure 5d, 60 mm extension), resulting in wider secondary thinning zone (spacing between boundary faults and the narrower central fault zone) than in the MAZ (Figure 5d, 60 mm extension; Figure 6i).

Overall, the MAZ localizes deformation, characterized by larger fault displacements (concentrated deformation) along a narrower and deeper deformation zone, whereas the FBZ accommodates deformation through a greater number of faults (distributed deformation) (Figures 5d and 6d), forming a wider and shallower rift. During the differential evolution of the two segments, no transfer faults develop in the northern margin.

Instead, displacement between segments is accommodated by variations in fault number and displacement magnitude.

5. Model MA-FAB-F (with pre-rift fabric between the two segments)
   Model MA-FAB-F takes into account the influence of the NNW–SSE pre-rift fault zone on the evolution of the northern continental margin of the SCS. During the initial extension stage (Figures 4e and 5e, 20 mm extension), faults exhibit first-order patterns similar to those in Model MA-FAB (Figures 4d and 5d, 20 mm extension). Notably, at this stage, the pre-existing NNW–SSE fabric (Figure 3c) is reactivated, producing small NNW-trending faults (Figures 4e and 5e, 20 mm extension). This NNW-trending fault zone experiences a relatively low degree of deformation during this stage (Figure 5e, 20 mm extension), interrupting along-strike continuity of the northern boundary faults. With further extension (Figures 4e and 5e, 40 mm extension), the NNW–SSE fault zone further reactivates, forming a NNW-trending subbasin at the northern boundary of the rift. Meanwhile, the southern boundary faults, similarly to those in Model MA-FAB (Figure 5d, 40 mm extension), develop along-strike offsets and become discontinuous at the heterogeneity conjunction (Figures 4e and 5e, 40 mm extension).

At the final extension stage (Figure 5e, 60 mm extension), the deformation zone deepens and widens. The fault number increases significantly, with FAB (L3) exhibiting notably more faults than the MAZ (L1) (Figure 6e). As in Model MA-FAB, the final results show that in the MAZ, the central depression undergoes intense thinning and rapid shallowing toward the narrow boundary subbasins, whereas in the FBZ, deformation is significantly wider and more distributed. The crust undergoes gentle thinning from the structure boundary to the center (Figure 5e, 60 mm extension). The NNW-trending subbasin further propagates northward, while being blocked by the central fault zone and ceasing at the northern boundary of the central fault. DEMs (Figure 5e, 60 mm extension) indicate that the tectonic activity along the western boundary faults of the NNW-trending fault zone is significantly more pronounced than along its eastern boundary faults. Unlike Model MA-FAB, where northern boundary faults adjust their number and orientation to accommodate differential displacement along strike caused by heterogeneity (Figure 5d, 60 mm extension), in Model MA-FAB-F, the orientation and number of boundary faults remain relatively consistent on both sides of the NNW-trending fault zone (Figure 5e, 60 mm extension).

Similar to Model MA-FAB, the secondary thinning zone in the FBZ of Model MA-FAB-F is broader than in the MAZ (Figure 6j). However, its width remains more stable and is narrower than in Model MA-FAB (Figure 6i), likely due to the influence of the NNW-trending subbasin. Model MA-FAB-F also features only minor secondary uplifts within the central fault zone, near the NNW-trending subbasin (Figure 5e, 60 mm extension). The central fault zone is more concentrated and nearly continuous in both the MAZ and the FBZ (Figure 5e, 60 mm extension) compared to Model MA-FAB (Figure 5d, 60 mm extension). Consequently, the central fault zone in the FAB of Model MA-FAB-F is wider than that in Model MA-FAB (Figures 5d vs. 5e, 60 mm extension), while the secondary thinning zone in FAB is narrower (Figure 6j).

The temporal evolution of Model MA-FAB-F (Figure 5e) reveals that structural segmentation develops early in the extension process, driven by along-strike changes in lithosphere structure and composition. Concurrently, the NNW-oriented pre-existing fabric influences the number of boundary faults and the width of the central depression zone. The differential evolution over time is clearly illustrated in animation sequences (Movie S5). The evolution of the other experiments is presented in Movies S1–S4.

4. Numerical Simulation

The analog modeling results effectively illustrate the differential evolution of the magmatic arc zone (MAZ) and forearc basin zone (FBZ) from a plan-view perspective, as well as the development of the transfer fault zone. However, due to the limitations of the four-layer analog models, it is challenging to obtain cross-sectional views of the internal structural evolution. To better analyze the along-section evolution of both the MAZ and FBZ, we developed 2D thermomechanical models for each domain (Figure 7, MAZ and FBZ) equivalent to the analog models (Figure 3). The numerical experiments were conducted using the open-source finite element code ASPECT (v2.4.0) (Gassmöller et al., 2018; Heister et al., 2017), which efficiently solves highly non-linear lithospheric deformation problems (Gouiza & Naliboff, 2021). This software employs the extended Boussinesq equations for momentum, mass, and energy (assuming an infinite Prandtl number) along with advection equations for each Eulerian compositional field (Glerum et al., 2020). For details regarding the governing equations, please refer to Naliboff et al. (2020) and Glerum et al. (2020).

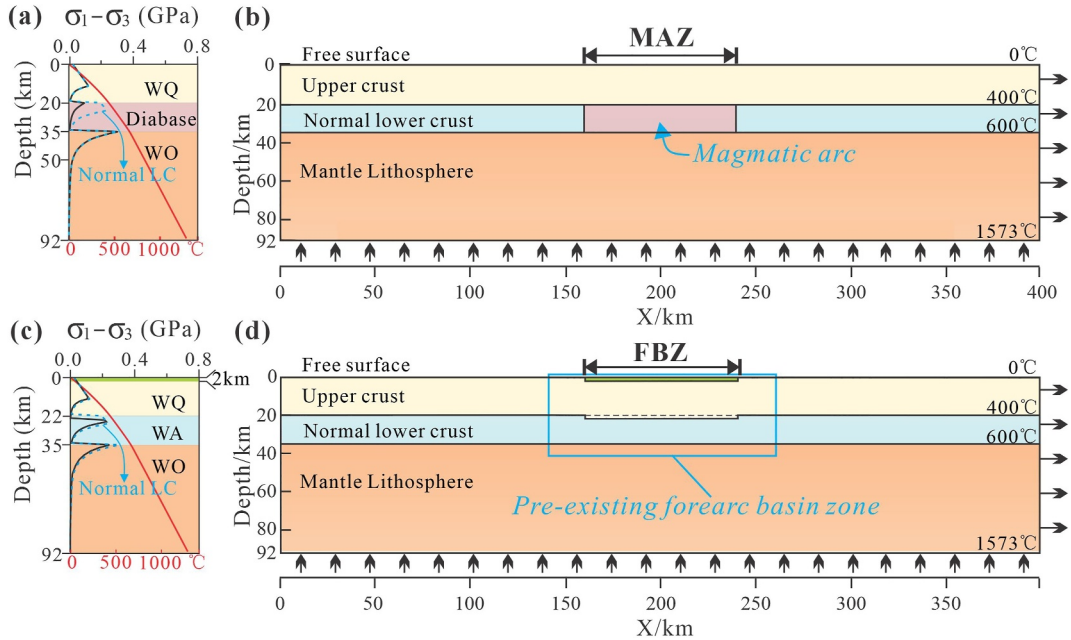

Figure 7. Lithospheric strength profiles and model setup illustrating the initial and boundary conditions. (a, c) Lithospheric strength and temperature profiles for the MAZ and FBZ. The blue dashed lines represent the lithospheric strength with a normal lower crust. (b, d) Model geometry, initial boundary conditions, and lithospheric structure. The magmatic arc represented by diabase, and the forearc basin characterized by a thinner lower crust are positioned at the center of the profile. Arrows on the right and at the bottom indicate the extension direction and inflow at the model base, respectively. WQ, wet quartzite; WA, wet anorthite; WO, wet olivine; LC, lower crust; MAZ, magmatic arc zone; FBZ, forearc basin zone.

4.1. Model Design

We set up a two-dimensional rectangular tectonic model in ASPECT with dimensions of 400 × 92 km (X and Z). Similar to the numerical model by Naliboff et al. (2020), the lithosphere contains three distinct compositional (lithologic) layers (Figure 7), representing the upper crust, lower crust, and mantle lithosphere. The rheological properties of these layers are defined by flow laws for wet quartzite (Rutter & Brodie, 2004), wet anorthite (Rybacki et al., 2006), and wet olivine (Hirth & Kohlstedt, 2004), respectively. Diabase was selected to represent the magmatic arc due to its lower strength compared to wet anorthite and its intrusive rock composition (Ranalli, 1997). Wet olivine was chosen to represent the mantle lithosphere, as it accurately reflects the low viscosity of the lithospheric mantle in the SCS region (Zhang & Wang, 2000; Zhang & Xiong, 2001). The modeled mantle lithosphere extends to the Lithosphere-Asthenosphere Boundary (LAB).

Based on analog modeling similarity principles, the geometric styles, extension velocity, and extension amount in the numerical models were determined. The lithosphere has a thickness of 92 km, with the upper and lower crusts being 20 and 15 km thick, respectively. The MAZ is represented as a 15 × 80 km rectangular domain. Similarly, the Mesozoic sediments in FBZ were scaled for numerical implementation and approximated as a 2 × 80 km rectangle, with properties identical to the upper crust. The initial model resolution is 1 km. Model parameters are detailed Table S1 in Supporting Information S1.

Deformation is driven by a consistent velocity of 5 cm/year toward the right (southwestward) around the center of the MAZ and FBZ, consistent with the velocity represented in the analog modeling. Lateral outflow is balanced by inflow at the model base, while the upper boundary is a free surface, and the front and back walls are free-slip boundaries.

Following the methodology of Naliboff et al. (2017, 2020), we generated an initial temperature profile representative of the continental lithosphere. The temperature distribution assumes a steady-state geotherm, considering the local thickness and material properties of compositional layers (e.g., density, thermal conductivity, and radioactive heating) (Glerum et al., 2020). The LAB is defined by a specific isotherm (1576 K).

10.1029/2024TC008541

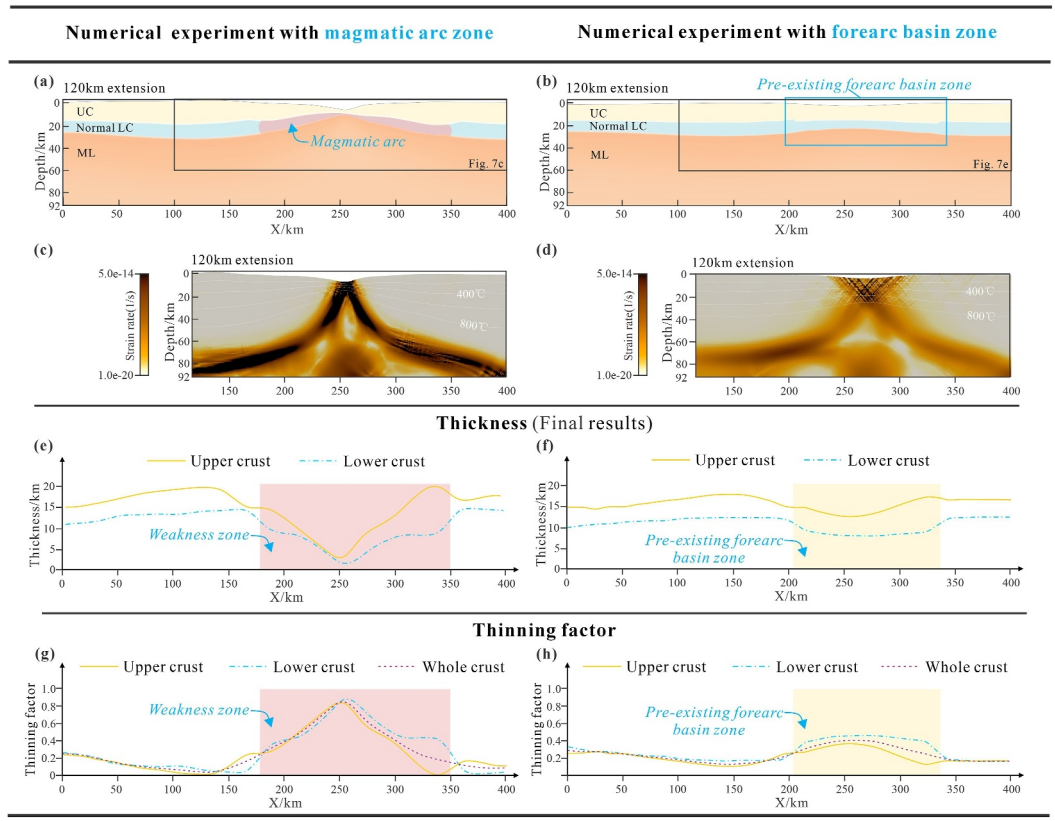

Figure 8. Numerical simulation results. (a, b) Material field after phases of deformation (120 km extension). (c, d) Strain rate field and thermal structure (contours in ∘C). (e, f) Diagram of the thickness variations in each lithospheric layer at the end of extension. (g, h) Thinning factors for upper and lower crusts at the end of extension, as well as for the whole crust. The thinning factor is calculated as (d0 – d)/d0, where d0 represents the constant initial thickness of the upper and lower crust. d represents the thickness of each layer after extension. UC, upper crust; LC, lower crust; ML, mantle lithosphere.

4.2. Numerical Modeling Results

The numerical experimental results are shown in Figure 8. In the MAZ, both the upper and lower crusts undergo intense thinning (Figure 8a), with their final thickness reduced to less than 5 km (Figure 8e). In contrast, in the FBZ, the thinner lower crust reduces crustal strength, resulting in moderate local thinning (Figure 8b). The FBZ exhibits a gentler thinning pattern (Figure 8f), with both the upper and lower crust remaining significantly thicker than in the MAZ (Figure 8e). Ultimately, necking uplifts are more pronounced in the MAZ than in the FBZ. The strain rate distribution further confirms that the MAZ experiences more concentrated and sharply thinned deformation (Figure 8c) compared to the FBZ (Figure 8d). In the MAZ, strain rates are highly localized and generally larger (Figure 8c), whereas in the FBZ, they are relatively smaller and more distributed (Figure 8d). These variations in crustal thickness and strain rate highlight a distinct segmentation in thinning characteristics between the MAZ and FBZ.

The thinning factor of each layer provides deeper insight into the lithospheric deformation behavior, particularly in terms of depth-dependent deformation. The thinning factors reveal distinct deformation patterns in the MAZ (Figure 8g) and FBZ (Figure 8h). In the MAZ, the thinning factor is significantly higher than in the adjacent normal lower crust, with the maximum whole crustal thinning factor reaching 0.9 (Figure 8g). Notably, the relative magnitude of the thinning factors for the upper and lower crust varies along the x-axis (Figure 8g). On the right flank (250 km $< x <$ 350 km), the thinning factor of the lower crust is significantly larger than that of the upper crust, whereas on the opposite side (150 km $< x <$ 250 km), the upper crust thinning factor is either slightly larger or even smaller than that of the lower crust (Figure 8g). In the FBZ, the lower crustal thinning factor is generally greater than that of the upper crust (Figure 8h). However, on the left flank (150 km $< x <$ 250 km), similar to the MAZ, the upper crustal thinning factor exceeds that of the lower crust, though this occurs over a

much smaller range. Both upper and lower crust thinning factors in FBZ are significantly smaller than those in the MAZ, with the maximum crustal thinning factor not exceeding 0.4 (Figure 8h). Full results of the rift process can be found in Movies S6 and S7.

5. Discussion

The experiments presented in the previous sections confirm the significant impact of lithospheric rheological layering and crustal heterogeneity on the structural evolution of and segmentation of rifted margins (Gouiza & Naliboff, 2021; Huismans & Beaumont, 2007; Molnar et al., 2017; Pérez-Gussinyé et al., 2023; Petri et al., 2019). In particular, variations in the thickness and rheology of heterogeneities (magmatic arc vs. forearc basin) result in substantial variations in depth-dependent thinning of the lithospheric layers. These findings provide critical insights into the Cenozoic thinning patterns along the northern SCS margin, highlighted in this section.

5.1. Role of Inheritance in Rifting and Margin Segmentation

Inherited structural features, created by previous tectonic and/or magmatic events, can reduce the static lithospheric strength prior to the rifting initiation. These pre-existing structures thereby influence the geometry of the nascent rift at scales ranging from an individual fault to lithospheric scale (Brune et al., 2023; Schiffer et al., 2020). Rifts typically nucleated and evolve preferentially within weaker lithospheric zones (Autin et al., 2013; Brune et al., 2017; Corti et al., 2007, 2022; Phillips et al., 2016, 2019; Yang et al., 2024; Zwaan et al., 2019, 2021, 2022). In this section, we analyze how initial lithospheric strength variations, controlled by crustal composition and thickness variations, influence differential extension, based on the results of our experiments, The reference experiment (Exp. R) (Figure 5a) demonstrates that in a laterally homogeneous lithosphere with a weak lithospheric mantle, deformation occurs in a distributed manner, with discontinuous faulting along the strike. Experiments with pre-existing heterogeneity that are homogeneous (single-factor experiments), exhibit a degree of segmentation, especially in the rift center, mainly expressed through discontinuities in fault strike and dip (e.g., Exp. MA, Figure 5b; Exp. FAB, Figure 5c). Similar observations were made by Naliboff et al. (2020), who highlighted that a first-order margin-scale segmentation may be naturally generated in all extensional settings without the need for specific inherited lithospheric anisotropies. However, the segmentation observed in these experiments cannot explain the major variations in Cenozoic crustal thinning patterns (Figure 1) (Hayes & Nissen, 2005; Franke et al., 2014; Zhao et al., 2019; J. Z. Zhang, Zhao, Ding, et al., 2023) or magmatic activity differences (McIntosh et al., 2014; Wang et al., 2006; Yan et al., 2001; J. Y. Zhang, Zhao, Sun, et al., 2023; J. Z. Zhang, Zhao, Ding, et al., 2023; Zhao et al., 2019) between the eastern and western segments of the northern SCS. Studies on margin segmentation in the North Atlantic (Schiffer et al., 2020), including the North Sea (Lenhart et al., 2019; Phillips et al., 2016), Norwegian continental margin (Gernigon et al., 2020; Naliboff et al., 2017; Osmundsen & Péron-Pinvidic, 2018; Péron-Pinvidic & Osmundsen, 2018) and Labrador Sea (Gouiza & Paton, 2019; Schiffer et al., 2022; Skaarup et al., 2006), have demonstrated that pre-existing heterogeneity along the rift axis is a key factor controlling structural style, thinning intensity, magmatic activity, and width of the rifted continental margin.

The models containing a magmatic arc (e.g., Exp. MA, Figure 5b; Exp. MA-FAB, Figure 5d; Exp. MA-FAB-F, Figure 5e) exhibit the lowest lithospheric strength and favors stress concentration. This is consistent with the previous findings (Autin et al., 2010, 2013; Brune et al., 2023; Corti, 2008; Corti et al., 2007, 2013; Fazlikhani et al., 2017; Mazur et al., 2021; Molnar et al., 2020; Petersen & Schiffer, 2016) showing that rifting initiates where lithospheric strength is lowest. Deformation in the MAZ is characterized by large fault displacements and a high concentration of faults (Figures 5b, 5d, and 5e). As a result, the rift center undergoes significant extension, becoming wider and deeper than the narrower and shallower boundary extension zones on both sides of the magmatic arc (Figures 5b, 5d, and 5e). The crust experienced rapid thinning from the boundary of the extension zone toward the rift center (Figures 6c, 6e, and 8a). The thinning factor of the lower crust in the MAZ is significantly higher (Figure 8g) compared to the FBZ (Figure 8h). This indicates that the pre-existing weak zone (magmatic arc) is a critical factor that can induce intense extension.

Different from the experiments with a weak magmatic arc, the experiments with a forearc basin (e.g., Exp. FAB, Figure 5c; Exp. MA-FAB, Figure 5d; Exp. MA-FAB-F, Figure 5e) exhibits more distributed and gradual thinning. The upper crustal thickness in the FBZ (Figure 8f) is greater than that in the MAZ (Figure 8e). No strain localization leads to intense brittle deformation in the FBZ (Figures 5c–5e). Instead, strain remains broadly

distributed (Figure 8d). This phenomenon can be attributed to two key factors: (a) The Mesozoic sediments in the forearc basin enhance the upper crustal strength, delaying strain localization. Previous studies (Olive et al., 2014, 2022) have demonstrated that thick sediments can delay the shifts in strain localization. (b) Although the thinner lower crust within the forearc basin reduces lithospheric strength (Figure 7c), it does not weaken as extensively as in the MAZ. Consequently, the forearc basin is less effective at concentrating strain compared to the MAZ.

Previous thermo-mechanical numerical modeling results have shown that ductile layers within the crust initiate deformation in a decoupled manner between the brittle crust and lithospheric mantle (Gouiza & Naliboff, 2021). Our experimental results indicate that in both the MAZ and FBZ, the crust exhibits similar decoupling behavior, influence by ductile layers with varying strengths, displaying depth-dependent thinning patterns. In both regions, the thinning factor of the lower crust is smaller on the left flank (150 km $< x <$ 250 km) of the profile, with some areas even exhibiting lower thinning factors than the upper crust (Figures 8g and 8h). In contrast, on the right flank (250 km $< x <$ 350 km), the thinning factor of the lower crust is significantly greater than the upper crust (Figures 8g and 8h). This asymmetry may be attributed to more pronounced thinning and flow of the lower crust on the right side during unilateral extension.

The experimental findings from both analog (Figures 4 and 5) and numerical (Figure 8) models highlight the role of lithospheric strength variations along strike in controlling segmentation characteristics in terms of thinning degree, deformation distribution, and lithospheric coupling. A comparative analysis of Model MA-FAB and Model MA-FAB-F further illustrates the influence of a pre-existing NNW-trending fabric (Figure 3c). In Exp. MA-FAB, differences in thinning patterns between the MAZ and FBZ are accommodated by varying the fault number (Figure 6i) and displacements (Figure 5d, 60 mm extension). Additionally, differential extension along the rift boundary is adjusted through fault bending at the northern boundary and fault offset at the southern boundary (Figure 5d, 60 mm extension). In contrast, Exp. MA-FAB-F (Figure 5e) demonstrates that reactivation of the pre-existing NNW-trending fabric serves as a transfer fault zone within the northern margin. Unlike Exp. MA-FAB (Figure 5d, 60 mm extension), where fault bending occurs at the northern boundary, Exp. MA-FAB-F instead develops a NNW-trending subbasin at the northern boundary to accommodate differential deformation (Figure 5e, 60 mm extension). The location and number of northern boundary faults on both sides of the NNW-trending subbasin remain consistent (Figure 5e, 60 mm extension). Additionally, this structure influences the formation of secondary structures (uplifts) within the central depression zone (Figures 5d and 5e, 60 mm extension), thereby affecting the width of the central rift zone in both the MAZ and FBZ. Consequently, this influences the width of the secondary thinning zones along the rift boundary (Figures 6i and 6j). Although the secondary thinning zone in the FAZ is wider than that in the adjacent MAZ in both experiments (Figures 6i and 6j), it is notably narrower in Exp. MA-FAB-F (Figure 6j) than in Exp. MA-FAB (Figure 6i). Fault offsets are also observed at the southern boundary in Exp. MA-FAB-F (Figure 5e, 60 mm extension).

In summary, in addition to the reactivation of pre-existing structures, which may led to rift segmentation (Corti, 2008; Corti et al., 2022; Heron et al., 2019; Maestrelli et al., 2020; Morley, 2017; Phillips et al., 2019; Pourhiet et al., 2017; Samsu et al., 2021; Zwaan & Schreurs, 2017; Zwaan et al., 2021, 2022), our findings demonstrate that variations in lithospheric compositional stratification exert a first-order control on the differential evolution of rift margin, such as thinning patterns, coupling, deformation zone width, and fault displacement. Additionally, a pre-existing fabric, oriented at a high angle to the heterogeneities, is reactivated during the rifting, serving as a transfer fault zone that regulates the rift segmentation.

5.2. Influence of the Lithospheric Heterogeneity on the Segmentation of the Northern SCS

In this section, we compare our analog modeling results (Exp. MA-FAB-F) and numerical simulations with the observed features along the northern SCS margin to investigate the role of pre-existing heterogeneity in controlling differential extensional features (Figure 9).

The experimental results indicate that the MAZ (northwestern segment) has experienced more intense deformation than the FBZ (northeastern segment) (Figures 5e and 6), resulting in significantly thinner crustal thickness in the MAZ (Figure 8e) compared to the FBZ (Figure 8f). This finding aligns with the 3D crustal P-wave seismic velocity model in the region (J. Z. Zhang, Zhao, Ding, et al., 2023), which suggests that tectonic deformation is less intense in the northeastern segment (J. Z. Zhang, Zhao, Ding, et al., 2023). The zone between the minimum elevation contour line (198 mm, derived from the planar digital elevation data; Figure 9a) and the main boundary faults (Figure 9a) corresponds to the moderate crustal thinning zone (15–20 km) defined along the northern SCS

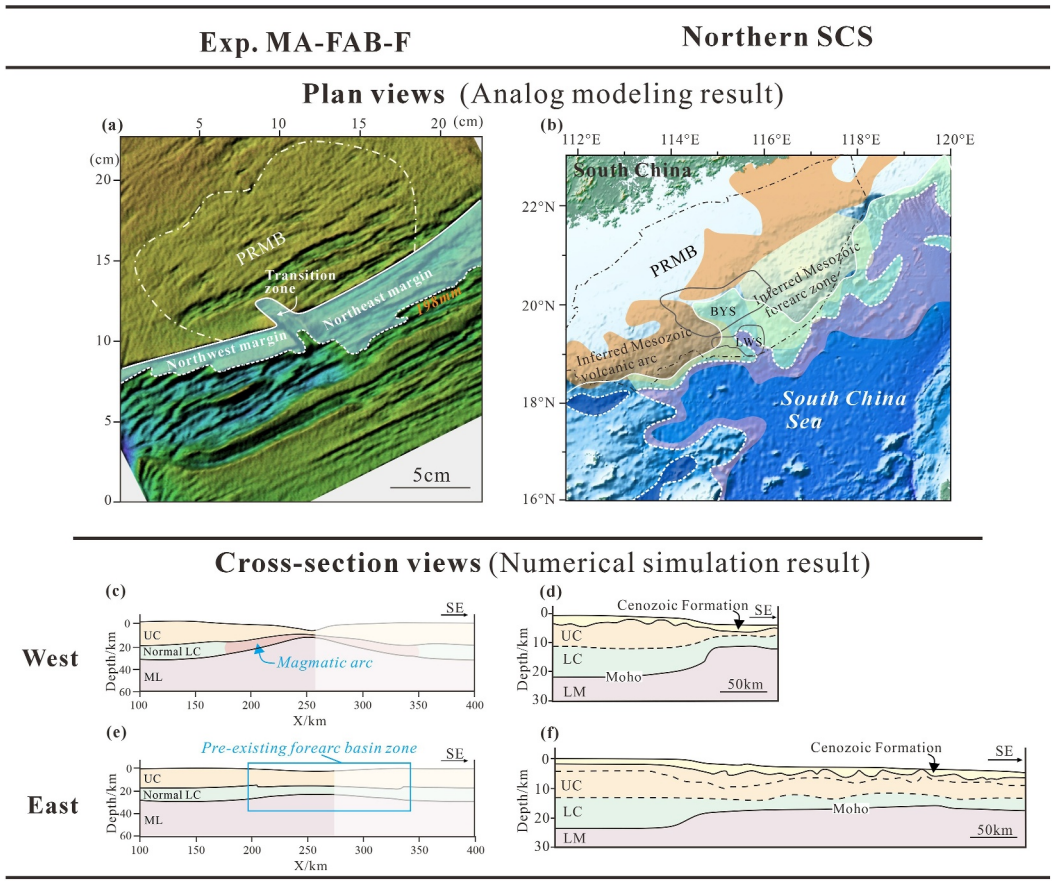

Figure 9. Comparison of plan-view and cross-sectional characteristics between the experimental results and the natural prototype. (a) End result of Exp. MA-FAB-F. The region between the minimum contour (198 mm) and the boundary faults is considered equivalent to the rifted margin. (b) Topography of the northern South China Sea margin. The highly extended continental crust (purple) is modified from Li et al. (2019). The area between crustal contours of 15 and 20 km (Li et al., 2019) is defined as the moderate extended continental crust (light green). PRMB, Pearl River Mouth Basin. BYS, Baiyun Sag. LWS, Liwan Sag. (c–f) Final results of numerical simulations (c, e) are compared with corresponding profiles in the natural prototype (d, f) (Li et al., 2019; Wang et al., 2006; Wu et al., 2012). The location of the observed profiles is shown in Figure 1a. The sections of experiment cropped from Figures 8a and 8b. UC, upper crust. LC, lower crust. LM, lithosphere mantle.

margin (Figure 9b). Both exhibit a pattern of being narrower in the northwest and wider in the northeast (Figures 9a and 9b), correlating with thinner (Figures 9c and 9d) and thicker (Figures 9e and 9f) crust, respectively.

The cross-section analyses also show similar characteristics as observed on the northern SCS margin. The crustal thinning along the northwestern margin of the SCS occurs rapidly from north to south, characterized by a wide proximal domain transitioning into a narrow necking and distal domain (Figure 9d) (Savva et al., 2014; Yang et al., 2018), while thinning in the northeastern segment is more gradual (Figure 9f). This phenomenon is also evident in our numerical simulations (Figures 9c and 9e). Our results indicate that the MAZ induces a pronounced necking effect, particularly with a sharp thinning of the lower crust (Figure 9c). The lateral migration of ductile materials (magmatic arc in this zone) below a thinner, brittle upper crust may account for the greater thinning of the lower crust (Corti, 2004; Petersen & Schiffer, 2016). Conversely, within the FBZ, deformation is more distributed and the thinning is relatively moderate (Figure 9e). The thinning factors along the basin profiles of the northern SCS reveal contrasting extension patterns between the upper crust and whole crust (Zhao et al., 2018). The northern flank displays an inverse extension discrepancy, where the thinning factor of the upper crust is greater than that of the lower crust. In contrast, the southern flank exhibits a positive extension discrepancy, with the lower crust thins more significantly than the upper crust (Zhao et al., 2018). This observation aligns with the

crust thinning trends observed in our numerical profiles (Figures 6h and 8g). Zhao et al. (2018) inferred that the inverse and positive crustal extension discrepancy may result from syn-rift landward directed lower crustal flow.

The pre-existing NW-trending fabric between the eastern and western segments is reactivated during extension, resulting in the formation of a NW-orientated subbasin (Figure 9a). The western boundary faults of this subbasin exhibit stronger activity than the eastern boundary faults (Figures 5e and 9a). This finding aligns with previous studies (Acocella et al., 1999; Brune et al., 2017), which suggest that in conditions of orthogonal rifting, the reactivation of pre-existing fabric depends on the angle between the rift margin and the boundaries of the pre-existing fabric. If this angle is greater than 90°, reactivation of its boundaries is favored; conversely, when the angle is less than 90°, reactivation is less probable. In our experiments, the western side of the pre-existing fabric is located in a region where the angle between the fabric and the rift zone is greater than 90° (105°, Figure 3c, Model MA-FAB-F), while the eastern side is where the angle is less than 90°. As a result, fault activity is stronger on the western side, explaining the variation in the activity of NW-trending faults in the Liwan Depression of the Pearl River Mouth Basin, where the western boundary faults exhibit greater activity (Zhao et al., 2019).

Our explanation elucidates the geometric segmentation characteristics of the northern SCS continental margin, such as crustal thickness, thinning width, and the variations in thinning factors. In addition, we clarify the impact of NNW- trending faults on the northern continental margin of the SCS. However, due to experimental limitations, our results cannot fully account for the current differences in magmatic activity between the northeastern and northwestern segments of the northern SCS (McIntosh et al., 2014; Wang et al., 2006; Yan et al., 2001; J. Y. Zhang, Zhao, Sun, et al., 2023; J. Z. Zhang, Zhao, Ding, et al., 2023; Zhao et al., 2019). These differences may result from a combination of factors, including pre-existing along-strike heterogeneity (Han et al., 2016; Li et al., 2018; Yan et al., 2014), mantle geochemistry (Sun et al., 2021; J. Z. Zhang, Zhao, Ding, et al., 2023), and the thermal state of the lithosphere (Clift, 2015; Nirrengarten et al., 2020; Shi et al., 2000). Further research, particularly incorporating 3D thermo-dynamic and thermomechanical modeling, is required to fully understand these differences.

6. Conclusion

The analog and numerical experiments in this study successfully simulated the complex interplay between pre-existing lithospheric rheological heterogeneity and the dynamics of continental rifting. The results indicate that in the western weak magmatic arc zone (MAZ), crustal deformation is highly localized and pronounced. In the eastern forearc basin zone (FBZ), however, rifting is more distributed resulting in a lower degree of crustal thinning.

The comparison between the experimental result (DEMs and thinning factors) and the observed features of the SCS margin confirms that the variations in lithospheric composition exert a first-order control on the northeast-northwest segmentation, which controlled the location of continental rupture, structural styles, sediment thickness, and rift width. The pre-existing fault zone between the northeastern and the northwestern segments was reactivated during extension acting as a transfer fault zone.

This study not only illuminates lithospheric rifting and inheritance along the northern SCS margin, but results are also applicable to other rifts and rifted margins worldwide, in particular concerning the role of lithospheric compositional stratification during continental rifting.

Data Availability Statement

The modeling software ASPECT (v2.4.0) can be obtained from GitHub at https://github.com/geodynamics/aspect/releases/tag/v2.4.0 (Bangerth et al., 2022); The input files to reproduce the data that support the findings in this study have been deposited in the GitHub repository https://github.com/yanggengxiong/Numerical-simulation-of-South-China-Sea (Yang, 2025a); Figures were made using ParaView, CorelDRAW and Python. The DEMs data from the analog modeling are available in the figshare repository https://figshare.com/s/22a8a7a339259469da0e (Yang, 2025b).

Acknowledgments
We sincerely thank Professor Stanislaw Mazur, the three anonymous reviewers, and the editors for their valuable and constructive comments, which have significantly contributed to the enhancement of our manuscript. We are also grateful to Professors Claudio Faccenna, Matthias Rosenau and Ernst Willingshofer for constructive discussions. This work was jointly supported by the National Natural Science Foundation of China (41927802, 42372264, 41972219), the National Science and Technology Major Project of China (2016ZX05026-002-007, 2016ZX05003-001), and the China Scholarship Council (202306190103).

References

Acocella, V., Faccenna, C., Funiciello, R., & Rossetti, F. (1999). Sand-box modelling of basement-controlled transfer zones in extensional domains. *Terra Nova*, *11*(4), 149–156. https://doi.org/10.1046/j.1365-3121.1999.00238.x

Autin, J., Bellahsen, N., Husson, L., Beslier, M.-O., Leroy, S., & D'Acremont, E. (2010). Analog models of oblique rifting in a cold lithosphere. *Tectonics*, *29*(6), TC6016. https://doi.org/10.1029/2010TC002671

Autin, J., Bellahsen, N., Leroy, S., Husson, L., Beslier, M., & D'Acremont, E. (2013). The role of structural inheritance in oblique rifting: Insights from analogue models and application to the Gulf of Aden. *Tectonophysics*, *607*, 51–64. https://doi.org/10.1016/j.tecto.2013.05.041

Bai, Y., Dong, D., Brune, S., Wu, S., & Wang, Z. (2019). Crustal stretching style variations in the northern margin of the South China Sea. *Tectonophysics*, *751*, 1–12. https://doi.org/10.1016/j.tecto.2018.12.012

Bai, Y., Wu, S., Liu, Z., Müller, R. D., Williams, S. E., Zahirovic, S., & Dong, D. (2015). Full-fit reconstruction of the South China Sea conjugate margins. *Tectonophysics*, *661*, 121–135. https://doi.org/10.1016/j.tecto.2015.08.028

Bangerth, W., Dannberg, J., Fraters, M., Gassmoeller, R., Glerum, A., Heister, T., et al. (2022). A parallel, extensible finite element code to simulate convection in both 2D and 3D models [Software]. *GitHub*. https://github.com/geodynamics/aspect/releases/tag/v2.4.0

Bellahsen, N., & Daniel, J. M. (2005). Fault reactivation control on normal fault growth: An experimental study. *Journal of Structural Geology*, *27*(4), 769–780. https://doi.org/10.1016/j.jsg.2004.12.003

Brun, J. P. (2002). Deformation of the continental lithosphere: Insights from brittle-ductile models. *Geological Society London Special Publications*, *200*(1), 355–370. https://doi.org/10.1144/GSL.SP.2001.200.01.20

Brune, S., Corti, G., & Ranalli, G. (2017). Controls of inherited lithospheric heterogeneity on rift linkage: Numerical and analog models of interaction between the Kenyan and Ethiopian rifts across the Turkana depression. *Tectonics*, *36*(9), 1767–1786. https://doi.org/10.1002/2017TC004739

Brune, S., Kolawole, F., Olive, J.-A., Stamps, D. S., Buck, W. R., Buiter, S. J. H., et al. (2023). Geodynamics of continental rift initiation and evolution. *Nature Reviews Earth & Environment*, *4*(4), 1–19. https://doi.org/10.1038/s43017-023-00391-3

Calignano, E., Sokoutis, D., Willingshofer, E., Brun, J. P., Gueydan, F., & Cloetingh, S. (2017). Oblique contractional reactivation of inherited heterogeneities: Cause for arcuate orogens. *Tectonics*, *36*(3), 542–558. https://doi.org/10.1002/2016TC004424

Chen, H. Z., Wu, X. J., Zhou, D., Wang, W. Y., & Hao, H. J. (2005). Meso-Cenozoic faults in Zhujiang River Mouth basin and their geodynamic background. *Journal of Tropical Oceanography*, *24*(2), 52–61. https://doi.org/10.3969/j.issn.1009-5470.2005.02.007

Cheng, J. H., Zhang, J. Z., Zhao, M. H., Du, F., Fan, C. Y., Wang, X. Y., & Qiu, X. L. (2021). Spatial distribution and origin of the high-velocity lower crust in the northeastern South China Sea. *Tectonophysics*, *819*, 229086. https://doi.org/10.1016/j.tecto.2021.229086

Childress, L. B., Alvarez Zarikian, C. A., Briais, A., Dadd, K. A., Deng, J.-M., & Höfig, T. W. (2020). Expedition 368X preliminary report: South China Sea rifted margin. *International Ocean Discovery Program*. https://doi.org/10.14379/iodp.proc.368X.101.2020

Clift, P. D. (2015). Coupled onshore erosion and offshore sediment loading as causes of lower crust flow on the margins of South China Sea. *Geoscience Letter*, *2*(1), 1–11. https://doi.org/10.1186/s40562-015-0029-9

Clift, P. D., Brune, S., & Quinteros, J. (2015). Climate changes control offshore crustal structure at South China Sea continental margin. *Earth and Planetary Science Letters*, *420*, 66–72. https://doi.org/10.1016/j.epsl.2014.10.008

Clift, P. D., Lin, J., & Barckhausen, U. (2002). Evidence of low flexural rigidity and low viscosity lower continental crust during continental break-up in the South China Sea. *Marine and Petroleum Geology*, *19*(8), 951–970. https://doi.org/10.1016/S0264-8172(02)00108-3

Clift, P. D., & Sun, Z. (2006). The sedimentary and tectonic evolution of the Yinggehai-Song Hong Basin and the southern Hainan margin, South China Sea: Implications for Tibetan uplift and monsoon intensification. *Journal of Geophysical Research*, *111*(B6), B06405. https://doi.org/10.1029/2005JB004048

Corti, G. (2008). Control of rift obliquity on the evolution and segmentation of the main Ethiopian rift. *Nature Geoscience*, *1*(4), 258–262. https://doi.org/10.1038/ngeo160

Corti, G., Bonini, M., Sokoutis, D., Innocenti, F., Manetti, P., Cloetingh, S., & Mulugeta, G. (2004). Continental rift architecture and patterns of magma migration: A dynamic analysis based on centrifuge models. *Tectonics*, *23*(2). https://doi.org/10.1029/2003TC001561

Corti, G., Iandelli, I., & Cerca, M. (2013). Experimental modeling of rifting at craton margins. *Geosphere*, *9*(1), 138–154. https://doi.org/10.1130/GES00863.1

Corti, G., Maestrelli, D., & Sani, F. (2022). Large-to local-scale control of pre-existing structures on continental rifting: Examples from the Main Ethiopian Rift, East Africa. *Frontiers in Earth Science*, *10*, 808503. https://doi.org/10.3389/feart.2022.808503

Corti, G., Wijk, J. V., Cloetingh, S., & Morley, C. K. (2007). Tectonic inheritance and continental rift architecture: Numerical and analogue models of the east African rift system. *Tectonics*, *26*(6), C6006. https://doi.org/10.1029/2006TC002086

Deng, H., Ren, J., Pang, X., Rey, P. F., McClay, K. R., Watkinson, I. M., et al. (2020). South China Sea documents the transition from wide continental rift to continental break up. *Nature Communications*, *4583*(1), 4583. https://doi.org/10.1038/s41467-020-18448-y

Dickinson, W. R. (1995). Forearc basins. In C. J. Busby & R. V. Ingersoll (Eds.), *Tectonics of sedimentary basins* (pp. 211–261). Blackwell Science.

Ding, W., & Li, J. (2016). Propagated rifting in the southwest sub-basin, South China Sea: Insights from analogue modelling. *Journal of Geodynamics*, *100*, 71–86. https://doi.org/10.1016/j.jog.2016.02.004

Ding, W., Li, J., Li, J., Fang, Y., & Tang, Y. (2013). Morphotectonics and evolutionary controls on the Pearl River Canyon system, South China Sea. *Marine Geophysical Researches*, *34*(3–4), 221–238. https://doi.org/10.1007/s11001-013-9173-9

Ding, W., Sun, Z., Mohn, G., Nirrengarten, M., Tugend, J., Manatschal, G., & Li, J. B. (2020). Lateral evolution of the rift-to-Drift transition in the South China Sea: Evidence from multi-channel seismic data and IODP Expeditions 367&368 drilling results. *Earth and Planetary Science Letters*, *531*, 115932. https://doi.org/10.1016/j.epsl.2019.115932

Fazlikhani, H., Fossen, H., Gawthorpe, R. L., Faleide, J. I., & Bell, R. E. (2017). Basement structure and its influence on the structural configuration of the northern North Sea rift. *Tectonics*, *36*(6), 1151–1177. https://doi.org/10.1002/2017TC004514

Franke, D. (2013). Rifting, lithosphere breakup and volcanism: Comparison of magma poor and volcanic rifted margins. *Marine and Petroleum Geology*, *43*, 63–87. https://doi.org/10.1016/j.marpetgeo.2012.11.003

Franke, D., Savva, D., Pubellier, M., Steuer, S., Mouly, B., Auxietre, J. L., et al. (2014). The final rifting evolution in the South China Sea. *Marine and Petroleum Geology*, *58*, 704–720. https://doi.org/10.1016/j.marpetgeo.2013.11.020

Frisch, W., Meschede, M., & Blakely, R. (2011). *Plate tectonics—continental drift and mountain building*. Springer. https://doi.org/10.1007/978-3-540-76504-2

Gassmöller, R., Lokavarapu, H., Heien, E., Puckett, E. G., & Bangerth, W. (2018). Flexible and scalable particle-in-cell methods with adaptive mesh refinement for geodynamic computations. *Geochemistry, Geophysics, Geosystems*, *19*(9), 3596–3604. https://doi.org/10.1029/2018GC007508

Gernigon, L., Franke, D., Geoffroy, L., Schiffer, C., Foulger, G. R., & Stoker, M. (2020). Crustal fragmentation, magmatism, and the diachronous opening of the Norwegian-Greenland Sea. *Earth-Science Reviews*, *206*, 102839. https://doi.org/10.1016/j.earscirev.2019.04.011

Glerum, A., Brune, S., Stamps, D. S., & Strecker, M. N. (2020). Victoria continental microplate dynamics controlled by the lithospheric strength distribution of the East African Rift. *Nature Communications*, *11*(1), 2881. https://doi.org/10.1038/s41467-020-16176-x

Gouiza, M., & Naliboff, J. (2021). Rheological inheritance controls the formation of segmented rifted margins in cratonic lithosphere. *Nature Communications*, *12*(1), 4653. https://doi.org/10.1038/s41467-021-24945-5

Gouiza, M., & Paton, D. A. (2019). The role of inherited lithospheric heterogeneities in defining the crustal architecture of rifted margins and the magmatic budget during continental breakup. *Geochemistry, Geophysics, Geosystems*, *20*(4), 1836–1853. https://doi.org/10.1029/2018GC007808

Graveleau, F., Hurtrez, J.-E., Dominguez, S., & Malavieille, J. (2011). A new experimental material for modeling relief dynamics and interactions between tectonics and surface processes. *Tectonophysics*, *513*(1–4), 68–87. https://doi.org/10.1016/j.tecto.2011.09.029

Hall, R. (2002). Cenozoic geological and plate tectonic evolution of SE Asia and the SW Pacific: Computer-based reconstructions, model and animations. *Journal of Asian Earth Sciences*, *20*(4), 353–431. https://doi.org/10.1016/S1367-9120(01)00069-4

Han, J., Xu, G., Li, Y., & Zhuo, H. (2016). Evolutionary history and controlling factors of the shelf breaks in the Pearl River Mouth basin, northern South China Sea. *Marine and Petroleum Geology*, *77*, 179–189. https://doi.org/10.1016/j.marpetgeo.2016.06.009

Hayes, D. E., & Nissen, S. S. (2005). The South China Sea margins: Implications for rifting contrasts. *Earth and Planetary Science Letters*, *237*(3–4), 601–616. https://doi.org/10.1016/j.epsl.2005.06.017

Heister, T., Dannberg, J., Gassmöller, R., & Bangerth, W. (2017). High accuracy mantle convection simulation through modern numerical methods – II: Realistic models and problems. *Geophysical Journal International*, *210*(2), 833–851. https://doi.org/10.1093/gji/ggx195

Heron, P., Peace, A., McCaffrey, K., Welford, K., Wilson, R., & Pysklywec, R. (2019). Segmentation of rifts through structural inheritance: Creation of the Davis strait. *Tectonics*, *38*. https://doi.org/10.31223/osf.io/6mkc8

Hirth, G., & Kohlstedt, D. (2004). Rheology of the upper mantle and the mantle wedge: A view from the experimentalists. In *Inside the subduction factory, geophysical monograph series*. https://doi.org/10.1029/138GM06

Huang, H., Klingelhoefer, F., Qiu, X., Li, Y., & Wang, P. (2021). Seismic imaging of an intracrustal deformation in the northwestern margin of the South China Sea: The role of a ductile layer in the crust. *Tectonics*, *40*(2), e2020TC006260. https://doi.org/10.1029/2020TC006260

Hubbert, M. K. (1937). Theory of scale models as applied to the study of geologic structures. *Geological Society of America Bulletin*, *48*(10), 1459–1519. https://doi.org/10.1130/GSAB-48-1459

Huismans, R. S., & Beaumont, C. (2007). Roles of lithospheric strain softening and heterogeneity in determining the geometry of rifts and continental margins. *Geological Society, London, Special Publications*, *282*(1), 111–138. https://doi.org/10.1144/SP282.6

Kato, M., & Jordan, T. H. (1999). Seismic structure of the upper mantle beneath the western Philippine Sea. *Physics of the Earth and Planetary Interiors*, *110*(3), 263–283. https://doi.org/10.1016/S0031-9201%2898%2900176-9

Kusznir, N. J., & Park, R. G. (1987). The extensional strength of the continental lithosphere: Its dependence on geothermal gradient, and crustal composition and thickness. *Geological Society, London, Special Publications*, *28*(1), 35–52. https://doi.org/10.1144/gsl.sp.1987.028.01.04

Larsen, H. C., Mohn, G., Nirrengarten, M., Sun, Z., Stock, J., Klaus, A., et al. (2018). Rapid transition from continental breakup to igneous oceanic crust in the South China Sea. *Nature Geoscience*, *11*(10), 782–789. https://doi.org/10.1038/s41561-018-0198-1

Lenhart, A., Jackson, C. A.-L., Bell, R. E., Duffy, O. B., Gawthorpe, R. L., & Fossen, H. (2019). Structural architecture and composition of crystalline basement offshore West Norway. *Lithosphere*, *11*(2), 273–293. https://doi.org/10.1130/L668.1

Li, C. F., Li, J. B., Ding, W. W., Fanke, D., Yao, Y., Shi, H., et al. (2015). Seismic stratigraphy of the central South China Sea basin and implications for neotectonics. *Journal of Geophysical Research*, *120*(3), 1377–1399. https://doi.org/10.1002/2014JB011686

Li, C. F., Xu, X., Lin, J., Sun, Z., Zhu, J., Yao, Y. J., et al. (2014). Ages and magnetic structures of the South China Sea constrained by deep tow magnetic surveys and IODP Expedition 349. *Geochemistry, Geophysics, Geosystems*, *15*(12), 4958–4983. https://doi.org/10.1002/2014GC005567

Li, F., Sun, Z., Pang, X., Liao, J., Yang, H., Xie, H., et al. (2019). Low-viscosity crustal layer controls the crustal architecture and thermal distribution at hyperextended margins: Modeling insight and application to the northern South China Sea margin. *Geochemistry, Geophysics, Geosystems*, *20*(7), 3248–3267. https://doi.org/10.1029/2019GC008200

Li, F., Sun, Z., & Yang, H. (2018). Possible spatial distribution of the Mesozoic volcanic arc in the present-day South China Sea continental margin and its tectonic implications. *Journal of Geophysical Research: Solid Earth*, *123*(8), 6215–6235. https://doi.org/10.1029/2017JB014861

Li, F. C., Sun, Z., Ding, W., Yang, H., Xie, H., Pang, X., et al. (2021). Compression induced anomalous subsidence in the extensional sedimentary basin: A numerical study from the Pearl River Mouth basin, northern South China Sea margin. *Geophysical Research Letters*, *48*(18), e2021GL094750. https://doi.org/10.1029/2021GL094750

Li, F. C., Sun, Z., Yang, H. F., Lin, J., Stock, J. M., Zhao, Z. X., et al. (2020). Continental interior and edge breakup at convergent margins induced by subduction direction reversal: A numerical modeling study applied to the South China Sea margin. *Tectonics*, *39*(11), e2020TC006409. https://doi.org/10.1029/2020TC006409

Li, H. L., Wu, Z. C., Ji, F., Gao, J. Y., Yang, C. G., Yuan, Y., et al. (2020). Crustal density structure of the northern South China Sea from constrained 3-D gravity inversion. *Chinese Journal of Gephysics*, *63*(5), 1894–1912. https://doi.org/10.6038/cjg2020NO064

Liu, J., Sun, Z., Wang, Z., Sun, Z., Zhao, Z., Wang, Z., et al. (2015). Tectonic differences between eastern and western sub-basins of the Qiongdongnan Basin and their dynamics. *Marine Geophysical Researches*, *36*(1), 61–79. https://doi.org/10.1007/s11001-014-9247-3

Maestrelli, D., Montanari, D., Corti, G., Del Ventisette, C., Moratti, G., & Bonini, M. (2020). Exploring the interactions between rift propagation and inherited crustal fabrics through experimental modeling. *Tectonics*, *39*(12), e2020TC006211. https://doi.org/10.1029/2020TC006211

Mao, Y., Li, Y., Yan, B., Wang, X., Jia, D., & Chen, Y. (2021). Response of surface erosion to crustal shortening and its influence on tectonic evolution in fold-and-thrust belts: Implications from sandbox modeling on tectonic geomorphology. *Tectonics*, *40*(5), e2020TC006515. https://doi.org/10.1029/2020TC006515

Mazur, S., Green, C., Stewart, M. G., Whittaker, J. M., Williams, S., & Bouatmani, R. (2012). Displacement along the Red River fault constrained by extension estimates and plate reconstructions. *Tectonics*, *31*(5). https://doi.org/10.1029/2012TC003174

Mazur, S., Malinowski, M., Maystrenko, Y. P., & Gągała, Ł. (2021). Pre-existing lithospheric weak zone and its impact on continental rifting–The Mid-Polish Trough, Central European Basin System. *Global and Planetary Change*, *198*, 103417. https://doi.org/10.1016/j.gloplacha.2021.103417

McIntosh, K., Lavier, L., van Avendonk, H., Lester, R., Eakin, D., & Liu, C. S. (2014). Crustal structure and inferred rifting processes in the northeast South China Sea. *Marine and Petroleum Geology*, *58*, 612–626. https://doi.org/10.1016/j.marpetgeo.2014.03.012

Molnar, N., Cruden, A., & Betts, P. (2020). The role of inherited crustal and lithospheric architecture during the evolution of the Red Sea: Insights from three-dimensional analogue experiments. *Earth and Planetary Science Letters*, *544*, 116377. https://doi.org/10.1016/j.epsl.2020.116377

Molnar, N. E., Cruden, A. R., & Betts, P. G. (2017). Interactions between propagating rotational rifts and linear rheological heterogeneities: Insights from three-dimensional laboratory experiments. *Tectonics*, *36*(3), 420–443. https://doi.org/10.1002/2016TC004447
Morley, C. K. (2012). Late cretaceous-early palaeogene tectonic development of SE Asia. *Earth-Science Reviews*, *115*(1–2), 37–75. https://doi.org/10.1016/j.earscirev.2012.08.002
Morley, C. K. (2017). The impact of multiple extension events, stress rotation and inherited fabrics on normal fault geometries and evolution in the Cenozoic rift basins of Thailand. *Geological Society, London, Special Publications*, *439*(1), 413–445. https://doi.org/10.1144/SP439.3
Naliboff, J., Buiter, S. J. H., Péron-Pinvidic, G., Osmundsen, P. T., & Tetrault, J. (2017). Complex fault interaction controls continental rifting. *Nature Communications*, *8*(1), 1179. https://doi.org/10.1038/s41467-017-00904-x
Naliboff, J. B., Glerum, A., Brune, S., Péron-Pinvidic, G., & Wrona, T. (2020). Development of 3-D rift heterogeneity through fault network evolution. *Geophysical Research Letters*, *47*(13), e2019GL086611. https://doi.org/10.1029/2019GL086611
Nestola, Y., Storti, F., & Cavozzi, C. (2015). Strain rate-dependent lithosphere rifting and necking architectures in analog experiments. *Journal of Geophysical Research: Solid Earth*, *120*(1), 584–594. https://doi.org/10.1002/2014JB011623
Nirrengarten, M., Mohn, G., Schito, A., Corrado, S., Gutiérrez-García, L., Bowden, S. A., & Despinois, F. (2020). The thermal imprint of continental breakup during the formation of the South China Sea. *Earth and Planetary Science Letters*, *531*, 115972. https://doi.org/10.1016/j.epsl.2019.115972
Olive, J.-A., Behn, M. D., & Malatesta, L. C. (2014). Modes of extensional faulting controlled by surface processes. *Geophysical Research Letters*, *41*, 6725–6733. https://doi.org/10.1002/2014GL061623
Olive, J.-A., Malatesta, L. C., Behn, M. D., & Buck, R. W. (2022). Sensitivity of rift tectonics to global variability in the efficiency of river erosion. *PNAS*, *119*(13), 2115077119. https://doi.org/10.1073/pnas.2115077119
Osmundsen, P. T., & Péron-Pinvidic, G. (2018). Crustal-scale fault interaction at rifted margins and the formation of domain-bounding breakaway complexes: Insights from offshore Norway. *Tectonics*, *37*(3), 935–964. https://doi.org/10.1002/2017TC004792
Pérez-Gussinyé, M., Collier, J. S., Armitage, J. J., Hopper, J. R., Sun, Z., & Ranero, C. R. (2023). Towards a process-based understanding of rifted continental margins. *Nature Reviews Earth & Environment*, *4*(3), 166–184. https://doi.org/10.1038/s43017-022-00380-y
Péron-Pinvidic, G., & Osmundsen, P. T. (2018). The Mid Norwegian – NE Greenland conjugate margins: Rifting evolution, margin segmentation, and breakup. *Marine and Petroleum Geology*, *98*, 162–184. https://doi.org/10.1016/j.marpetgeo.2018.08.011
Petersen, K. D., & Schiffer, C. (2016). Wilson cycle passive margins: Control of orogenic inheritance on continental breakup. *Gondwana Research*, *39*, 131–144. https://doi.org/10.1016/j.gr.2016.06.012
Petri, B., Duretz, T., Mohn, G., Schmalholz, S. M., Karner, G. D., & Müntener, O. (2019). Thinning mechanisms of heterogeneous continental lithosphere. *Earth and Planetary Science Letters*, *512*, 147–162. https://doi.org/10.1016/j.epsl.2019.02.007
Phillips, T. B., Fazlikhani, H., Gawthorpe, R. L., Fossen, H., Jackson, C. A. L., Bell, R. E., et al. (2019). The influence of structural inheritance and multiphase extension on rift development, the Northern North Sea. *Tectonics*, *38*(12), 4099–4126. https://doi.org/10.1029/2019TC005756
Phillips, T. B., Jackson, C. A. L., Bell, R. E., Duffy, O. B., & Fossen, H. (2016). Reactivation of intrabasement structures during rifting: A case study from offshore southern Norway. *Journal of Structural Geology*, *91*, 54–73. https://doi.org/10.1016/j.jsg.2016.08.008
Pichot, T., Delescluse, M., Chamot-Rooke, N., Pubellier, M., Qiu, Y., Meresse, F., et al. (2014). Deep crustal structure of the conjugate margins of the SW South China Sea from wide-angle refraction seismic data. *Marine and Petroleum Geology*, *58*, 627–643. https://doi.org/10.1016/j.marpetgeo.2013.10.008
Pourhiet, L. L., May, D. A., Huille, L., Watremez, L., & Leroy, S. (2017). A genetic link between transform and hyper-extended margins. *Earth and Planetary Science Letters*, *465*, 184–192. https://doi.org/10.1016/j.epsl.2017.02.043
Ranalli, G. (1997). Rheology and deep tectonics. *Annals of Geophysics*, *40*(3). https://doi.org/10.4401/ag-3893
Ren, J. Y., Xiong, P., Peng, Y. U., Chao, L., & Pan, L. (2018). Characteristics and formation mechanism of deepwater and ultra-deepwater basins in the northern continental margin of the South China Sea. *Chinese Journal of Geophysics*, *61*(12), 4901–4920. https://doi.org/10.6038/cjg2018L0558
Rutter, E. H., & Brodie, K. H. (2004). Experimental grain size-sensitive flow of hot-pressed Brazilian quartz aggregates. *Journal of Structural Geology*, *26*(11), 2011–2023. https://doi.org/10.1016/j.jsg.2004.04.006
Rybacki, E., Gottschalk, M., Wirth, R., & Dresen, G. (2006). Influence of water fugacity and activation volume on the flow properties of fine-grained anorthite aggregates. *Journal of Geophysical Research*, *111*(B3), B03203. https://doi.org/10.1029/2005JB003663
Samsu, A., Cruden, A. R., Molnar, N. E., & Weinberg, R. F. (2021). Inheritance of penetrative basement anisotropies by extension-oblique faults: Insights from analogue experiments. *Tectonics*, *40*(5), e2020TC006596. https://doi.org/10.1029/2020TC006596
Santimano, T., & Pysklywec, R. (2020). The influence of lithospheric mantle scars and rheology on intraplate deformation and orogenesis: Insights from tectonic analog models. *Tectonics*, *39*(5). https://doi.org/10.1029/2019TC005841
Savva, D., Pubellier, M., Franke, D., Chamot-Rooke, N., Meresse, F., Steuer, S., & Auxietre, J. L. (2014). Different expressions of rifting on the South China Sea margins. *Marine and Petroleum Geology*, *58*, 579–598. https://doi.org/10.1016/j.marpetgeo.2014.05.023
Schiffer, C., Doré, A. G., Foulger, G. R., Franke, D., Geoffroy, L., Gernigon, L., et al. (2020). Structural inheritance in the North Atlantic. *Earth-Science Reviews*, *206*, 102975. https://doi.org/10.1016/j.earscirev.2019.102975
Schiffer, C., Peace, A. L., Jess, S., & Rondenay, S. (2022). The crustal structure in the Northwest Atlantic region from receiver function inversion–Implications for basin dynamics and magmatism. *Tectonophysics*, *825*, 229235. https://doi.org/10.1016/j.tecto.2022.229235
Shao, L., Cao, L., Qiao, P., Zhang, X., Li, Q., & van Hinsbergen, D. J. (2017). Cretaceous–Eocene provenance connections between the Palawan continental terrane and the northern South China Sea margin. *Earth and Planetary Science Letters*, *477*, 97–107. https://doi.org/10.1016/j.epsl.2017.05.008
Shao, L., You, H., Hao, H., Wu, G., Qiao, P., & Lei, Y. (2007). Petrology and depositional environments of Mesozoic strata in the northeastern South China Sea. *Geological Review*, *53*(2), 164–170. [in Chinese with English Abstract]. https://doi.org/10.1016/S1872-5791(07)60044-X
Shi, X., Burov, E., Leroy, S., Qiu, X. L., & Xia, B. (2005). Intrusion and its implication for subsidence: A case from the Baiyun Sag, on the northern margin of the South China Sea. *Tectonophysics*, *407*, 117–134. https://doi.org/10.1016/j.tecto.2005.03.008
Shi, X., Zhou, D., & Zhang, Y. (2000). Lithospheric thermal-rheological structures of the continental margin in the northern South China Sea. *Chinese Science Bulletin*, *45*(22), 2107–2112. https://doi.org/10.1007/BF03183537
Skaarup, N., Jackson, H. R., & Oakey, G. (2006). Margin segmentation of Baffin Bay/Davis Strait, eastern Canada based on seismic reflection and potential field data. *Marine and Petroleum Geology*, *23*(1), 127–144. https://doi.org/10.1016/j.marpetgeo.2005.06.002
Sokoutis, D., & Willingshofer, E. (2011). Decoupling during continental collision and intra-plate deformation. *Earth and Planetary Science Letters*, *305*(3–4), 435–444. https://doi.org/10.1016/j.epsl.2011.03.028
Stock, J. M., Sun, Z., Klaus, A., Larsen, H. C., Jian, Z., Alvarez Zarikian, C. A., et al. (2018). Site U1500. *Proceedings of the International Ocean Discovery Program*, 367–368. https://doi.org/10.14379/iodp.proc.367368.104.2018

Sun, Z., Li, F. C., Lin, J., Sun, L. T., Pang, X., & Zheng, J. Y. (2021). The rifting-breakup process of the passive continental margin and its relationship with magmatism: The attribution of the South China Sea. *Earth Science*, *46*(3), 770–789. https://doi.org/10.3799/dqkx.2020.371

Sun, Z., Lin, J., Qiu, N., Jian, Z. M., Wang, P. X., Pang, X., et al. (2019). The role of magmatism in the thinning and breakup of the South China Sea continental margin. *National Science Review*, *6*(5), 871–876. https://doi.org/10.1093/nsr/nwz116

Sun, Z., Pang, X., Zhong, Z. H., Zhou, D., Chen, C. M., Hao, H. J., et al. (2005). Dynamics of Tertiary tectonic evolution of the Baiyun Sag in the Pearl River Mouth basin. *Earth Science Frontiers*, *12*(4), 489–498. https://doi.org/10.1360/gs050303

Sun, Z., Stock, J., Jian, Z., McIntosh, K., Alvarez-Zarikian, C. A., & Klaus, A. (2016). Expedition 367/368 scientific prospectus: South China Sea rifted margin. *International Ocean Discovery Program*. https://doi.org/10.14379/iodp.sp.367368.2016

Sun, Z., Stock, J. M., Klaus, A., Larsen, H. C., Jian, Z., Alvarez Zarikian, C. A., et al. (2018). Site U1499. *Proceedings of the International Ocean Discovery Program*, 367–368. https://doi.org/10.14379/iodp.proc.367368.103.2018

Suo, Y. H., Li, S. Z., Jin, C., Zhang, Y., Zhou, J., Li, X. Y., et al. (2019). Eastward tectonic migration and transition of the Jurassic-Cretaceous Andean-type continental margin along Southeast China. *Earth-Science Reviews*, *196*, 102884. https://doi.org/10.1016/j.earscirev.2019.102884

Tong, H., Meng, L., Cai, D., Wu, Y., Li, X., & Liu, M. (2009). Fault formation and evolution in rift basins—Sandbox modeling and cognition. *Acta Geologica Sinica*, *83*(6), 759–774. https://doi.org/10.1016/S1874-8651(10)60080-4

Tsai, C.-H., Hsu, S.-K., Yeh, Y.-C., Lee, C.-S., & Xia, K. (2004). Crustal thinning of the northern continental margin of the South China Sea. *Marine Geophysical Researches*, *25*(1–2), 63–78. https://doi.org/10.1007/s11001-005-0733-5

Wan, X., Li, C. F., Zhao, M., He, E., Liu, S., Qiu, X., et al. (2019). Seismic velocity structure of the magnetic quiet zone and continent-ocean boundary in the northeastern South China Sea. *Journal of Geophysical Research: Solid Earth*, *124*(11), 11866–11899. https://doi.org/10.1029/2019JB017785

Wang, Q., Zhao, M. H., Zhang, J. Z., Zhang, H. Y., Sibuet, J. C., Li, Z. Z., et al. (2023). Breakup mechanism of the northern South China Sea: Evidence from the deep crustal structure across the continent-ocean transition. *Gondwana Research*, *120*, 47–69. https://doi.org/10.1016/j.gr.2022.09.004

Wang, T. K., Chen, M.-K., Lee, C.-S., & Xia, K. (2006). Seismic imaging of the transitional crust across the northeastern margin of the South China Sea. *Tectonophysics*, *412*(3–4), 237–254. https://doi.org/10.1016/j.tecto.2005.10.039

Wang, Y., Fan, W., Zhang, G., & Zhang, Y. (2012). Phanerozoic tectonics of the South China block: Key observations and controversies. *Gondwana Research*, *22*(1), 806–818. https://doi.org/10.1016/j.gr.2012.02.019

Weijermars, R., & Schmeling, H. (1986). Scaling of Newtonian and non-Newtonian fluid dynamics without inertia for quantitative modelling of rock flow due to gravity (including the concept of rheological similarity). *Physics of the Earth and Planetary Interiors*, *43*(4), 316–330. https://doi.org/10.1016/0031-9201(86)90021-X

Wu, G., Wang, R., Hao, H., & Shao, L. (2007). Microfossil evidence for development of marine Mesozoic in the north of South China Sea [in Chinese with English Abstract]. *Marine Geology & Quaternary Geology*, *27*(1), 79–85.

Wu, J., & Suppe, J. (2018). Proto-South China Sea plate tectonics using subducted slab constraints from tomography. *Journal of Earth Sciences*, *29*(6), 1304–1318. https://doi.org/10.1007/s12583-017-0813-x

Wu, Z. L., Li, J. B., Ruan, A. G., Lou, H., Ding, W. W., Niu, X. W., & Li, X. B. (2012). Crustal structure of the northwestern sub-basin, South China Sea: Results from a wide-angle seismic experiment. *Science China Earth Sciences*, *55*(1), 159–172. https://doi.org/10.1007/s11430-011-4324-9

Yan, P., Wang, L., & Wang, Y. (2014). Late Mesozoic compressional folds in Dongsha Waters, the northern margin of the South China Sea. *Tectonophysics*, *615*, 213–223. https://doi.org/10.1016/j.tecto.2014.01.009

Yan, P., Zhou, D., & Liu, Z. (2001). A crustal structure profile across the northern continental margin of the South China Sea. *Tectonophysics*, *338*, 1–21. https://doi.org/10.1016/S0040-1951(01)00062-2

Yang, G., Yin, H., Gan, J., Wang, W., Zhu, J., Jia, D., et al. (2022). Explaining structural difference between the eastern and western zones of the qiongdongnan basin, northern South China Sea: Insights from scaled physical models. *Tectonics*, *41*(2), e2021TC006899. https://doi.org/10.1029/2021TC006899

Yang, G., Yin, H., Gan, J., Wang, W., Zhu, J., Jia, D., et al. (2024). Structural segmentation in the Qiongdongnan Basin, South China Sea: Insights from analogue models and implications for hydrocarbon exploration. *AAPG Bulletin*, *108*(5), 907–941. https://doi.org/10.1306/01162422069

Yang, G. X. (2025a). Numerical models of the northern South China Sea [Dataset]. *GitHub*. https://github.com/yanggengxiong/Numerical-simulation-of-South-China-Sea

Yang, G. X. (2025b). DEMs data from the analog modeling [Dataset]. *Figshare*. https://figshare.com/s/22a8a7a339259469da0e

Yang, L., Ren, J., McIntosh, K., Pang, X., Lei, C., & Zhao, Y. (2018). The structure and evolution of deepwater basins in the distal margin of the northern South China Sea and their implications for the formation of the continental margin. *Marine and Petroleum Geology*, *92*, 234–254. https://doi.org/10.1016/j.marpetgeo.2018.02.032

Zahirovic, S., Seton, M., & Müller, R. D. (2014). The Cretaceous and Cenozoic tectonic evolution of Southeast Asia. *Solid Earth*, *5*(1), 227–273. https://doi.org/10.5194/se-5-227-2014

Zhang, J., & Wang, J. Y. (2000). Deep geodynamic characteristics of tectonic expansion in the northern margin of the South China Sea. *Science in China - Series D: Earth Sciences*, *30*(6), 561–567. https://doi.org/10.1360/zd2000-30-6-561

Zhang, J., & Xiong, L.-P. (2001). The characteristics and mechanism of geodynamic evolution of the South China Sea. *Chinese Journal of Geophysics*, *44*(5), 602–610. https://doi.org/10.1002/cjg2.179

Zhang, J. Y., Zhao, M. H., Sun, Z., Sun, L. T., Xu, M., Yang, H. F., et al. (2023). Large volume of magma involved in South China Sea rifting: Implication for mantle breakup earlier than crust. *Tectonophysics*, *853*, 229801. https://doi.org/10.1016/j.tecto.2023.229801

Zhang, J. Z., Zhao, M., Ding, W., Ranero, C. R., Sallares, V., Gao, J., et al. (2023). New insights into the rift-to-drift process of the northern South China Sea margin constrained by a three-dimensional wide-angle seismic velocity model. *Journal of Geophysical Research: Solid Earth*, *128*(4), e2022JB026171. https://doi.org/10.1029/2022JB026171

Zhao, F., Alves, T. M., Xia, S., Li, W., Fan, C., Mi, L., et al. (2019). Along-strike segmentation of the South China Sea margin imposed by inherited pre-rift basement structures. *Earth and Planetary Science Letters*, *530*, 115862. https://doi.org/10.1016/j.epsl.2019.115862

Zhao, Z., Sun, Z., Liu, J., Pérez-Gussinyé, M., & Zhuo, H. (2018). The continental extension discrepancy and anomalous subsidence pattern in the western Qiongdongnan Basin, South China Sea. *Earth and Planetary Science Letters*, *501*, 1–13. https://doi.org/10.1016/j.epsl.2018.08.048

Zhou, D., Ru, K., & Chen, H. Z. (1995). Kinematics of Cenozoic extension on the South China Sea continental margin and its implications for the tectonic evolution of the region. *Tectonophysics*, *251*(1–4), 161–177. https://doi.org/10.1016/0040-1951(95)00018-6

Zhou, D., Sun, Z., Chen, H. Z., Xu, H. H., Wang, W. Y., Pang, X., et al. (2008). Mesozoic paleogeography and tectonic evolution of South China Sea and adjacent areas in the context of Tethyan and paleo-Pacific interconnections. *Island Arc*, *17*(2), 186–207. https://doi.org/10.1111/j.1440-1738.2008.00611.x

Zwaan, F., Chenin, P., Erratt, D., Manatschal, G., & Schreurs, G. (2021). Complex rift patterns, a result of interacting crustal and mantle weaknesses, or multiphase rifting? Insights from analogue models. *Solid Earth*, *12*(7), 1473–1495. https://doi.org/10.5194/se-12-1473-2021

Zwaan, F., Chenin, P., Erratt, D., Manatschal, G., & Schreurs, G. (2022). Competition between 3D structural inheritance and kinematics during rifting: Insights from analogue models. *Basin Research*, *34*(2), 824–854. https://doi.org/10.1111/bre.12642

Zwaan, F., & Schreurs, G. (2017). How oblique extension and structural inheritance influence rift segment interaction: Insights from 4D analog models. *Interpretation*, *5*(1), SD119–SD138. https://doi.org/10.1190/INT-2016-0063.1

Zwaan, F., & Schreurs, G. (2023). Analog models of lithospheric-scale rifting monitored in an X-ray CT scanner. *Tectonics*, *42*(3), e2022TC007291. https://doi.org/10.1029/2022TC007291

Zwaan, F., Schreurs, G., & Buiter, S. J. H. (2019). A systematic comparison of experimental set-ups for modelling extensional tectonics. *Solid Earth*, *10*(4), 1063–1097. https://doi.org/10.5194/se-10-1063-2019